Numerical simulations of waves passing over a slope



Zhenhao Li

St Cross College

University of Oxford

A thesis submitted for the degree of

Master of Science

Michaelmas 2022

Numerical simulations of waves passing over a slope

A thesis submitted for the degree of
Master of Science at the University of Oxford

By Zhenhao Li, St Cross College, Michaelmas 2022

Extreme waves have been studied for decades in terms of the problems such as the formation of the extreme waves and the underestimate of the probability of extreme waves by the standard models in the open ocean. There are different mechanisms exist to explain extreme waves and one of the possible mechanisms is waves propagation over an abrupt depth transition. It is found that the statistical distribution of waves can be modified when they propagate over sharp discontinuities in the bathymetry. According to the experimental results, the statistics of the waves in the experiments and the Gaussian model contradict considerably, and the distribution of surface elevation significantly deviates from the Gaussian distribution when waves propagate over sharp discontinuities. After lots of studies on this problem, it is found that this mismatch is contributed by strong nonlinear effects, which can result in errors when only using the law of superposition and Gaussian model to evaluate the waves. Thus, investigation on how the abrupt depth transition provokes extreme waves becomes important to understand the extreme waves for the safety design of offshore infrastructures.

One mechanism to explain the relationship between the extreme waves and the abrupt depth transition is the interaction between second-order bound waves and free waves released due to the abrupt depth transitions. Another mechanism is that sea-states are pushed out of equilibrium. In our work, we not only analyze the progress of wave propagation over an abrupt depth transition, but also study the wave kinematics after the top of the slope. We emphasize that all of the slopes or abrupt depth transitions mentioned in this thesis are rising slopes (i.e. waves propagate from deeper water side to shallower water side). Because the wave kinematics is also important as the wave loading on offshore structures is mainly determined by the wave kinematics as well as the dynamics. For practical engineering purposes, wave loading is closely related to the safety of engineering design.

In this study, a thorough convergence test and validation for the numerical code (OceanWave3D) is conducted. The wave propagation over the abrupt depth transitions is analyzed for unidirectional wave groups, unidirectional random waves, and directional spreading wave groups. The wave kinematics after the top of the slope is investigated, and the wave loading on the offshore structures is evaluated. In addition, we analyze the angle of the second-order released waves when directional spreading waves propagating over the abrupt depth transitions.

Acknowledgements

Firstly, I would like to thank my supervisors professor Thomas Adcock and professor Ton van den Bremer. Throughout my research they have provided deep theoretical and practical insight, and substantial encouragement. They have been a source of many suggestions. I have benefited immensely from the experience of the last two years and the many opportunities that they have offered me, and for that I am most grateful.

I would like to thank Dr. Tianning Tang for kindly teaching me to use OceanWave3D and joining the weekly meeting. In addition, I would like to thank for his patience and kindness. He has always provided me a lot of help during my study. I am grateful to Dr. Mike kendall for providing supports during my studies at St Cross College and his encouragement behind my decision to embark on my study.

I would like to thank Dr. Yan Li and Samuel Draycott for kindly providing the experimental data, which contains the propagation of wavegroups and random waves over an abrupt depth transitions. In addition, I would like to thank their background literature on the explanation of mechanism of the relationship between the abrupt depth transition and the rouge waves.

A special thanks must go to the following friends: Claire Shi, William Wei, Tim Tang, Yuxuan Liu, Qian xiao, Yuri Seung, Jude Fletcher who have brought a necessary mix of tolerance, support and enjoyment to my studies at Oxford.

My greatest thanks go to my family for their encouragement and support throughout my studies. My mother's unconditional love and faith in a completion to this project has been truly inspiring and most important to the final achievement.

Contents

1 Introduction **1**

1.1 The ocean environment 1
1.2 Offshore engineering design challenges 3
1.3 Aims and Main Findings 4
1.4 Methodology and Overview 6

2 Literature Review **8**

2.1 Basic concepts 8
2.1.1 Wave statistics 8
2.1.2 Wave spectrum 12
2.2 Linear wave theory 14
2.2.1 Hydrodynamic problem 14
2.2.2 Kinematics 15
2.2.3 Dynamics 16
2.2.4 Wave energy 17
2.3 Wave propagating on a variable bathymetry 18
2.3.1 Waves over gentle changes in bathymetry (linear shoaling) . . 18
2.3.2 Statistical deviations from Gaussian model 20
2.3.3 Wave propagation over a bar 21
2.3.4 Evidence for the rogue waves at the top of an abrupt depth transition 21
2.3.5 Theories to explain the influence of the depth transition 25
2.3.6 Changes to the shape of average extreme events 26
2.4 Wave loading on cylinders 27
2.5 Introduction to OceanWave3D 28
2.5.1 Code description 28
2.5.2 Formulation of the problem 30

2.5.3 Wave generation and absorption 31

3 On Rogue Waves Generated by Abrupt Depth Transitions 34
3.1 Abstract 34
3.2 Introduction 35
3.3 Methodology 36
3.3.1 Numerical simulations by OW3D 36
3.3.2 Experimental data and set-up 40
3.4 Verification 40
3.4.1 Convergence on flat bathymetry 40
3.4.2 Convergence on varying bathymetry 44
3.5 Validation: comparison with experimental data 46
3.6 Kinematics of wave over variable bathymetry 49
3.7 Conclusions 52

4 Wave loads on ocean infrastructure increase as a result of waves passing over abrupt depth transitions 54
4.1 abstract 54
4.2 Introduction 55
4.3 Numerical and experimental methodology 56
4.3.1 Experimental setup 56
4.3.2 Numerical set up 57
4.3.3 Input waves 59
4.4 Validation against experiments 60
4.5 Results 68
4.6 Conclusions 72

5 Directionally spread wave groups propagating over an abrupt depth transition 74
5.1 Introduction 74
5.2 Numerical methodology 76
5.2.1 Numerical set up 76
5.2.2 Input waves 79
5.3 Results 81
5.3.1 Theories to explain the angle of the second-order released waves 81
5.3.2 Numerical results of directionally spread waves 85
5.4 Conclusions 89

6 Conclusions and Recommendations **90**
6.1 The convergence test and validation of OceanWave3D 91
6.2 The analysis of wave kinematics and wave loading on the structures . 92
6.3 The analysis of the angle of the release second-order free waves. 93
6.4 Recommendations for the future work 94
6.4.1 Analysis of directionally spread random waves 94
6.4.2 Analysis of wave kinematics for directionally spread random waves 94

References **96**

A Governing equations for OW3D **106**

List of Figures

2.1 Comparison between experimental and theoretical average shape of extreme events at different locations. x indicates the distance to the top of the slope, and positive value means location after the slope. t is time, and η is the surface elevation, f is the peak frequency, and Slope is the gradient of the seabed slope. 26

3.1 Diagram of experimental set-up including gauges, step, beach and wave-maker positions (from Li et al. (2021a)). 39

3.2 Convergence test of different parameters in OW3D for (a, b) Δt, (c, d) Δx, and (e, f) N_z. Parameters are also non-dimensionalised by wave-length (λ) or wave period (T). Δt is the time interval between two time steps. Δx is the spatial interval between two nodes on the x-axis. N_z is the total number of nodes on the z-axis. $T/\Delta t$ is time steps per wave period and $\lambda/\Delta x$ is nodes per wave-length. norm is the vector norm of the difference between the case of interest and the base case. norm_0 is the vector norm of the base case. η_{max} is the maximum surface elevation. 41

3.3 Reversibility of OW3D simulation, for (a) the relationship between the gradient of slope and the numerical difference, for (b, c, d, e) the comparison between the wave group at the start of the forward case and at the end of the backward case in different slopes. $\text{norm}/\text{norm}_0$ is the ratio between the vector norm of difference and the vector norm of the wave group at the start of the forward case; η is the surface elevation and t is time. 45

3.4 Comparison between numerical wave groups and experimental wave groups at different gauges. Comparison between the spectrum of numerical and experimental results for (a, b, c), for (d, e, f) the comparison between experimental wave group and numerical wave group generated using two relaxation zones and one itertaion, for (g, h, i) the first-order harmonics, for (j, k, l) the second-order harmonics and for (m, n, o) the third-order harmonics. η is the surface elevation and f_0 is the peak frequency. t is time, and x indicates the distance to the top of the slope. 47
3.5 Total velocity (m/s) at different horizontal and vertical location at t=31.6 s. x and z represent horizontal and vertical locations. The magnitude of the total velocity corresponds to different colors, shown in colorbar. 50
3.6 Maximum value of the envelope of the moment (M_{max}) at different spatial location (x) for a cylinder whose diameter is 0.5 m. The top of the slope 21.88 m. In the nonlinear case, nonlinear terms of the free-surface boundary conditions are included in the simulation, and in the linear case, numerical waves follow linear wave theory. 51

4.1 Diagram of experimental set-up including gauges, step, beach and wave-maker positions (from Li et al. (2021b)). 57
4.2 Representative time histories of surface elevation at different gauges comparing experimental and numerical result (1:1 slope case), where x indicates the distance from the top of the slope, η the surface elevation and t time. 61
4.3 The significant wave height H_s at different gauges for numerical and experimental results (1:1 slope case) 63
4.4 Comparison of experimental and simulated wave height statistics with 90% confidence intervals at gauge 1, 3, 8 and 11 for the 1:1 slope case. Wave heights (H) are normalised by the significant wave height (H_s) 65
4.5 Average of the 40 large crests normalised by the value at the largest crest for the 1:1 slope case with 90% confidence intervals, where t is the time relative to the largest crest and x indicates the distance from the top of the slope 67

4.6 Comparison of moment statistics for slope 1:1 and slope 1:3 at gauge 3 and 8. Two gauges are shown with 90% confidence intervals. Moment is the total moment around the sea-bed after the slope. 69
4.7 Overturning moment about the sea-bed predicted by the numerical model. 90% confidence intervals are shown. The moment is the moment corresponding to the probability of 0.1% (one-in-1000 wave) in the moment exceedance figure for different spatial locations. The locations of gauge 3 (At the top of the slope) and gauge 8 (0.9 m after the top of the slope) are indicated by dotted black lines. 71

5.1 Figure of the slope (a) and the top view of the slope (b) for α = 53° slope with $H_{shallow}$ = 50 m case. α indicates the angle of the slope with respect to the x-direction in the (x, y) plane. z indicates the water depth to the mean water level. Yellow region corresponds to the shallower-water side, and blue region is the deeper-water side 78
5.2 Initial condition for the surface elevation for the wave group in OceanWave3D, where η is the surface elevation. 80
5.3 Release-time theory to calculate the angle between the released second-order free wave and the x-direction, β_1. α indicates the angle of slope with x-direction in (x, y) plane. L_1 is the propagation distance on the deeper-water side and L_2 is the propagation distance on the shallower-water side. 82
5.4 Theory of Li *et al.*, the angle relation in terms of the angle of second-order bound waves before and after the slope and the angle of second-order released waves. $2k_{1,0,}+$ and θ_1 is the wavenumber and the angle of the second-order bound wave before the slope, respectively. $2k_{2,0,}+$ and θ_2 is the wavenumber and the angle of the second-order bound wave after the slope, respectively. $\kappa_{2,0,}+$ is the wavenumber of the second-order released free wave and θ_{2f} is the angle between the second-order released wave and the directional normal to the slope in the (x, y) plane. 82

5.5 The comparison of the theoretical angle of the released second-order free wave calculated by release-time theory (a) and Li *et al.* (b). $H_{shallow}$ is the water depth on the shallower-water side. α is the angle of the slope with the x-direction in the (x, y) plane. β_1 and β_2 are the angle of the released second-order free wave with the x-direction in the (x, y) plane, calculated by release-time theory and Li *et al.*, respectively. $\Delta\beta$ in (c) is the difference of the angle of the released second-order free wave calculated by these two theories ($\Delta\beta = \beta_1 - \beta_2$). 84

5.6 Contour plot of the initial condition. Slope is indicated by the black line. The contour plot is in an interval of surface elevation η between -0.5 m to 0.5 m. Arrow indicates the moving direction. 86

5.7 Contour plot of the numerical result of 1600_{th} timestep for 53° angle slope with 50 m $H_{shallow}$ case. β indicates the angle between the released second-order free wave and the x-direction in the (x, y) plane (top view of the waves). Slope is indicated by the black line. The contour plot is in an interval of surface elevation η between -0.5 m to 0.5 m. Arrow indicates the moving direction. 87

5.8 The comparison of the angle of the released second-order free waves calculated by numerical simulation, release-time theory or Li *et al.* α is the angle of the slope with the x-direction in the (x, y) plane and β is the angle of the released second-order free wave in the (x, y) plane. $H_{shallow}$ is the water depth on the shallower-water side. 88

List of Tables

1.1 Overview of different methodologies applied in this study. The angle of the slope in chapter 5, shown in bracket, is the angle between the slope and the x-direction in the (x, y) plane. 6

3.1 Different values of Δt, Δx and N_z in OW3D and their corresponding nodes per wave-length ($\lambda/\Delta x$) or time steps per wave period ($T/\Delta t$). 37
3.2 Variation of CFL number in OW3D when using different values of Δt and Δx =7.5 m to calculate the CFL number. 38
3.3 Length of the numerical domain L_x, number of nodes on the x-axis N_x, time duration of the simulation t, time interval between two time steps Δt, number of nodes on the z-axis N_z, non-dimensional depth in shallower water kd_s, non-dimensional depth in deeper water kd_d and wave-length λ. 38
3.4 The locations of gauges 1, 3, 8 and 11 in the experiment. Position x indicates the distance to the top of the slope, and positive value indicates gauges after the top of the slope (from Li et al. (2021a)). . . 40

4.1 The locations of 16 gauges in the experiment. Position x indicates the distance to the top of the slope, and positive value indicates gauges after the top of the slope (from Li et al. (2021a)). 57
4.2 Significant wave height (H_s) of numerical (1:1 slope case) and experimental results at gauge 1, 3, 8 and 11 63

5.1 Details of the different slopes and different bathymetry in the simulations by OW3D 77

Chapter 1

Introduction

1.1 The ocean environment

In maritime history, many stories are told of rogue waves with considerably larger crests, or heights, than the surrounding sea-state, as well as the destruction of engineering structures in the marine caused by such waves (Slocum, 1917; Draper, 1971; Liu, 2007). For example, in 1916, large waves with wave height up to 21 meters caused extreme damage to the United States Navy cruiser USS Memphis in Santo Domingo harbour (Roorda, 2019). In this accident, 40 people were killed and more than 204 people were injured. In the autumn of 1995, the Queen Elizabeth 2 encountered a large wave during passage of hurricane Luis (Haver, 2001). According to the ship's master, "It looked as though the ship was heading straight for the white cliffs of Dover," and, "there seemed to be two waves in succession as the ship fell into the 'hole' behind the first one". The wave height of second wave was approximately 30 m, whereas the average wave height of the sea was only 18 m. This gigantic wave also caused broken windows at 22 m above the mean water level. Numerous documents record large waves from sailors' testimonies and evidence of damages on ships. For example, MS München, a six-year-old barge carrier, sank at mid-Atlantic (Müller

et al., 2005). After the rescue team arrived, they found twisted attachment pins of an unreleased lifeboat, which were stored at 20 m above the water line. This damage was believed to be caused by violent force from extreme waves. In addition, rogue waves were believed to be a contributing factor to many accidents, such as the destruction of more than 22 super-carriers between 1969 and 1994 (Kharif and Pelinovsky, 2003).

Rogue waves have been defined using various criteria and need to be determined by significant wave height (H_s). Significant wave height can be defined as the mean of the highest one-third of waves or four times the standard deviation of the surface elevation, which can be calculated based on wave spectrum. Rogue waves are often defined as waves whose wave heights are 2 times larger than the significant wave height or wave crests are 1.25 times larger than the significant wave height (Dysthe et al., 2008):

$$\frac{\eta_c}{H_s} > 1.25 \quad \text{or} \quad \frac{H}{H_s} > 2, \tag{1.1}$$

in which η_c and H are the crest elevation and wave height of the rogue waves. A wave that satisfies either criterion can be regarded as a rogue wave for both narrow-banded spectrum and broad-banded spectrum.

Rogue waves have also been measured in the field, such as the Draupner (Haver, 2004), Andrea (Karin Magnusson and Donelan, 2013), and Killard (Flanagan et al., 2016) waves. Some possible mechanisms have been proposed to explain the occurrences of rogue waves on the surface of ocean in the last decades (Dysthe et al., 2008; Onorato et al., 2013; Adcock and Taylor, 2014). Wave propagation over an abrupt depth transition is one mechanism to explain the rogue waves and was identified by Trulsen et al. (2012), which has motivated many researchers. Over the past decades, wave propagation over an abrupt depth transition has received considerable attention and has been extensively investigated (Sergeeva et al., 2011; Trulsen et al., 2012; Gramstad et al., 2013; Bolles et al., 2019; Zheng et al., 2020). The studies on abrupt

depth transitions have implications for the engineering design as many offshore structures, such as fixed wind turbines, are often located at the top of a slope.

1.2 Offshore engineering design challenges

Investigation of rogue waves is important as it influences engineering design. For example, when it comes to the design of oil platforms, it is crucial to make sure the "air gap" between the sea level and the deck is enough to guarantee the wave cannot hit the deck and hence cause serious damage to the platform (Adcock and Taylor, 2014). Thus, the accurate estimation of the size and return period of rogue waves becomes important. For ships and floating platforms, the period and shape of large wave can determine the stability, thus it is important to evaluate not just the amplitude but also their shape (Adcock and Taylor, 2014). Due to the global energy crisis and greenhouse effect, renewable energies such as wind energy and tidal energy, are expected to be widely used in order to reduce the carbon dioxide emission. The wave loading on the structures and the avoidance of direct impact on wind turbine blades influences the design of offshore wind turbines. The forces or moments caused by waves on the structure become important, which can determine the life span of these mechanical facilities.

Investigating wave propagation over abrupt depth transitions is important as it can not only contribute to explaining rogue waves, but also influences engineering design. Many offshore structures are located at a top of an abrupt depth transition and the design of these structures is closely related to the evaluation of the wave loading on the structures caused by the rogue waves. Abrupt depth transitions exist in the form of natural and man-made bathymetric features, such as seamounts, continental shelves, steep beaches, reefs, and breakwaters. Abrupt depth transitions can lead to release of the free waves (Massel, 1983), transfer energy to higher frequencies (Beji

and Battjes, 1993) and, as shown recently, induce rogue waves (Trulsen et al., 2012; Zheng et al., 2020). The probability of a rogue wave has a local increase at the top of the abrupt depth transition (a rising slope), which has significant implications for the loading on structures placed at the top of the abrupt depth transition.

Apart from the investigation of wave height, studying the wave kinematics and wave loading after the top of the abrupt depth transition is also important for the design of offshore structures. Horizontal force from waves can dominate the base shear and the overturning moment on structures. In addition, offshore wind turbines have natural frequencies two or three times larger than the period of storm waves and low damping ratios particularly when turbines are parked during storms (Arany et al., 2016). Thus, the dynamic response on the offshore wind turbines such as the 'ringing' effect is important (Zang et al., 2010; Grue, 2011). In order to accurately analyze the dynamic response, the better description on the kinematics of extreme events is essential. The average shape of extreme events is also important when calculating the response of the ship and wave slamming effects for extreme events.

1.3 Aims and Main Findings

The aim of this study is to investigate both unidirectional waves and directionally spread waves propagating over an abrupt depth transition. The relationship between the abrupt depth transitions and the rogue waves is investigated, with the analysis of the wave kinematics under the free surface. The objectives of this work are:

1. To evaluate the accuracy of numerical results calculated by OceanWave3D when simulating waves passing over abrupt depth transitions and validate the numerical results against experimental measurements, which can also give a criterion to other researchers when using OceanWave3D to study this problem;

2. To analyze the waves kinematics under the free surface after the top of the

slope and explain how this alters wave loading;

3. To analyze the angle of the released second-order free waves when directionally spread waves pass over the abrupt depth transitions, as a starting point for the studying of directional waves.

In this respect, the main findings of this work are:

1. Convergence tests for numerical setup of OceanWave3D simulations are conducted and the accuracy of numerics for problems with variable bathymetry are validated against experimental results. We found that OceanWave3D is numerically accurate for simulating wave propagation over an abrupt depth transition with accurate reproduction of wave surface elevation profiles and statistics when compared against the experimental results for both wave groups and random waves cases.

2. The wave loading after the top of the slope is enhanced by the non-linear physics. This enhancement lasts for several wavelengths after the abrupt depth transitions. In addition, the enhanced overturning moments has an increase of approximately 20% for a variety of steep slopes compared with cases without considering the non-linear physics (cases simulated by linear version of OceanWave3D). Extra care is needed when designing ocean infrastructure at the top of the slope.

3. The released second-order free waves can be observed after the top of the slope when simulating the directionally spread waves passing over abrupt depth transitions. The slope is not uniform in the y-direction, leading to an angle with the x-direction in the (x, y) plane (top view of the slope). The angle of the released second-order free waves is mainly dominated by the angle between the slope and the x-direction in the (x, y) plane and is less influenced by the water depth on the shallower-water side, at least for the range of water depth considered herein. In addition, the agreement between our numerical results and two theoretical models is good.

1.4 Methodology and Overview

Chapter	Methods	Slope type	Wave type
3. On Rogue Waves Generated by Abrupt Depth Transitions	Numerical simulation (1D)	·1:1 slope	Unidirectional wave groups
4. Wave loads on Ocean infrastructure increases as a result of waves passing over abrupt depth transitions	Numerical simulation (1D)	·1:1 slope ·1:3 slope	Unidirecitonal random waves
5. Directionally spread waves propagates over abrupt depth transitions	Numerical simulation (2D)	·1:1 slope (33°) ·1:1 slope (41°) ·1:1 slope (53°) ·1:1 slope (71°)	Directionally spread wave groups

Table 1.1: Overview of different methodologies applied in this study. The angle of the slope in chapter 5, shown in bracket, is the angle between the slope and the x-direction in the (x, y) plane.

In order to study the relationship between the abrupt depth transitions and the probability of the rogue waves, three different types of wave are simulated, which are shown in Table 1.1. In chapter 3, we simulate the propagation of unidirectional wave groups over a 1:1 slope. We examine the accuracy of OceanWave3D with convergence test and validate the code against experimental results. We also analyze the wave kinematics under the free surface and calculate the moment on the offshore structures. In chapter 4, we focus on the evolution of unidirectional random waves over two different slopes, including a 1:1 slope and a 1:3 slope. We study the exceedance probability of wave height, average shape of extreme events. In terms of the wave kinematics, we utilise the overturning moment as an convenient metric to demonstrate the impact of abrupt depth transition on the wave kinematics. We show the moment corresponding to the probability of 0.1% (one-in-1000 wave) at different spatial locations based on the moment exceedance probability. In chapter 5, we simulate the propagation of directionally spread wave groups over slopes with different angles to the mean wave propagation direction (x-direction). There are four different angles between the slope

and the x-direction in the (x, y) plane, which are 33°, 41°, 53° and 70°. However, in all of the simulations, the slope along the x-direction is 1:1. We analyze the angle of released second-order free waves in each simulation.

This thesis is an 'integrated' one, i.e. the technical chapters are a collection of 'papers' rather than traditional chapters. Chapter 3 was published and presented at Ocean, Offshore and Arctic Engineering Conference (OMAE) (Li et al., 2022b). Chapter 4 has been accepted for publication in the Journal of Ocean Engineering and Marine Engineering (Li et al., 2022c). Chapter 5 has not been submitted for publication.

Chapter 2

Literature Review

2.1 Basic concepts

2.1.1 Wave statistics

In random-phase/amplitude model, an observation is treated as one realisation of a stochastic process (Barber and Ursell, 1948). Based on this assumption, the random-phase/amplitude model can be used to derive the wave amplitude spectrum, in which the surface elevation $\underline{\eta}(t)$ is regarded as the sum of a large number of harmonic waves, each with a constant amplitude and a phase randomly chosen for each realisation of the time record. Thus, the surface elevation at one location, with duration D, can be described as:

$$\underline{\eta}(t) = \sum_{i=1}^{N} \underline{a}_i \cos(2\pi f_i t + \underline{\alpha}_i), \tag{2.1}$$

in which $\underline{a}_i$, and $\underline{\alpha_i}$ correspond to the amplitude and phase, respectively, of each frequency $f_i = i/D$ (i =1, 2, 3, $\cdots$; the frequency interval is therefore $\Delta f = 1/D$). The underscore means that the variable is a random variable. The value of the amplitude of each harmonic wave ($\underline{a}_i$) depends on its probability density function. For one of

the harmonic waves, once the value of the amplitude is determined, the amplitude of this harmonic wave is constant, and this harmonic wave is one of the components of the wave record. N indicates that the wave is regarded as the sum of N harmonics waves, and t represents time.

The phases and amplitudes, being random variables, can be obtained from their respective probability density functions. In this model, phase at each frequency f_i is uniformly distributed from 0 to 2π, and the probability density function of the phase $p(\alpha_i)$ can be expressed by:

$$p(\alpha_i) = \frac{1}{2\pi}, \quad 0 < \alpha_i \leq 2\pi. \tag{2.2}$$

The probability density function of the amplitude $p(a_i)$ at each frequency is determined by parameter μ_i, which is the expected value of the amplitude $\mu_i = E\{\underline{a}_i\}$:

$$p(a_i) = \frac{\pi}{2}\frac{a_i}{\mu_i^2}\exp\left(-\frac{\pi a_i^2}{4\mu_i^2}\right), \quad a_i \geq 0. \tag{2.3}$$

In 'short-term' statistics, the surface elevation spectrum is assumed to be statistically stationary, and the free surface is described by a Gaussian process (Cartwright and Longuet-Higgins, 1956). The instantaneous surface elevation is Gaussian distributed, and the mean is zero $E\{\underline{\eta}\} = 0$. The probability density function of instantaneous surface elevation is given by:

$$p(\eta) = \frac{1}{(2\pi m_0)^{1/2}}\exp\left(-\frac{\eta^2}{2m_0}\right), \tag{2.4}$$

in which m_0 is the zeroth-order moment (i.e. variance of the surface elevation, η). Moments of spectrum play an important role in defining wave parameters. Many statistical characteristics are derived from the variance density spectrum $S(f)$ by using the moments of the spectrum. The n^{th} spectral moment is given by:

$$m_n = \int_0^\infty f^n S(f) \mathrm{d}f. \tag{2.5}$$

If the value of n is 0, it corresponds to m_0 (zeroth-order moment), and the value of m_0 is equal to the variance of surface elevation:

$$\text{variance} = E\{\underline{\eta}^2\} = \int_0^\infty S(f) \mathrm{d}f = m_0. \tag{2.6}$$

Wave period parameters can also be derived from the wave spectrum by calculating the probability that $\underline{\eta}(t)$ is below $\eta = 0$ or the fraction of time that $\underline{\eta}(t)$ is below $\eta = 0$ (Cavanie et al., 1976). Thus, the mean zero-crossing period $\overline{T}_0$ can be calculated by zeroth-order moment and second-order moment (Rice, 1944):

$$\overline{T}_0 = \sqrt{\frac{m_0}{m_2}}. \tag{2.7}$$

In the narrowbanded limit, the value of the crest is always positive, and the total number of the crests is equal to the total number of the zero-up-crossing points. Based on this, the total number of crests which are higher than a specific value η ($\underline{\eta}_{\text{crest}} > \eta$) can be estimated, and the probability density function of $\underline{\eta}_{\text{crest}}$ can be derived as:

$$p_{\underline{\eta}_{\text{crest}}}(\eta) = \frac{\eta}{m_0} \exp\left(-\frac{\eta^2}{2m_0}\right). \tag{2.8}$$

According to this equation, the probability density function of crests is also related to the zeroth-order moment, and it follows the Rayleigh distribution. However, for a broader spectrum, the waves are more irregular, and the crest height might be negative, which means the number of the crest is not equal to the number of zero-up-crossing, and the distribution of the crest is also influenced. The spectral width can be quantified with a parameter ε defined by Cartwright and Longuet-Higgins (1956)

as:

$$\varepsilon = \left(1 - \frac{m_2^2}{m_0 m_4}\right)^{1/2}. \tag{2.9}$$

For waves with a narrow spectrum in deep water, the height of the wave is practically equal to twice the crest height. Based on the probability density function of crest, the probability density function of wave height $p(H)$ can be derived, which also follows Rayleigh distribution,

$$p(H) = \frac{H}{4m_0} \exp\left(-\frac{H^2}{8m_0}\right). \tag{2.10}$$

In addition, the significant wave height, calculated by the average height of the highest one-third of wave heights, can also be derived from the cumulative distribution function for wave height,

$$H_s = 4\sqrt{m_0}. \tag{2.11}$$

We should also consider the probability of a particular crest height being exceeded. $\Pr\{\underline{\eta}_{\text{crest}} > \eta\}$ describes the probability if we randomly choose a crest in a stationary sea state, and this crest height exceeds a level of surface elevation (η). We set $Q_{\text{crest}} = \Pr\{\underline{\eta}_{\text{crest}} > \eta\}$, and choose all crest heights from a wave record. The probability that all crest heights in duration D are smaller than a certain level η is given by:

$$\Pr\{\text{all}\,\underline{\eta}_{\text{crest}} \leq \eta\}_D = (1 - Q_{\text{crest}})^N, \tag{2.12}$$

in which N is the total number of crests in duration D. If all crest heights are smaller than the level η, then the maximum crest height ($\underline{\eta}_{\text{max,crest}}$) and all of the surface elevations ($\underline{\eta}$) or the maximum surface elevation ($\underline{\eta}_{\text{max}}$) should be smaller than this level (η), so that:

$$\begin{aligned}\Pr\left\{ \text{ all } \underline{\eta}_{\text{crest}} < \eta \right\}_D &= \Pr\left\{ \underline{\eta}_{\text{max, crest}} < \eta \right\}_D = \Pr\{ \text{ all } \underline{\eta} < \eta \}_D \\ &= \Pr\{ \underline{m}_{\text{max}} < \eta \}_D = \Pr\{\eta < \eta\}_D = (1 - Q_{\text{crest}})^N\end{aligned} \tag{2.13}$$

Thus, the probability that one or more crest height is larger than this level (η) can be expressed as:

$$\Pr\{\underline{\eta}_{\text{max,crest}} > \eta\} = 1 - (1 - Q_{\text{crest}})^N. \tag{2.14}$$

The cumulative distribution function of maximum individual wave height can be obtained by similar process as the derivation of maximum crest height. $\Pr\{\underline{H} > H\}$ describes the probability if we randomly choose a wave height in a stationary sea state, and this height exceeds a level of H. We set $Q_H = \Pr\{\underline{H} > H\}$. The probability of the maximum wave height is smaller than a certain value of wave height (H) is given by:

$$\Pr\{\underline{H}_{\text{max}} \leq H\} = (1 - Q_H)^N. \tag{2.15}$$

where N is the total number of wave heights. The calculation of the probability of the maximum wave height can be applied to both narrow-banded spectrum and broad-banded spectrum.

2.1.2 Wave spectrum

The wave spectrum is a standard tool to describe the state of ocean waves. It describes sea surface as a stochastic process instead of a single observation of the sea surface. A single observation can only be regarded as one realisation of the stochastic process. Thus, wave spectrum represents all possible observations, which could occur under the specific conditions of the actual observation.

In a given amplitude spectrum, we can create one realisation of $\underline{\eta}(t)$ by determining the values of the phase ($\underline{\alpha}_i$) and amplitude ($\underline{a}_i$) from their probability density functions (shown in equation (2.2) and equation (2.3), respectively). A wave record of field data thus can be regarded as a specific realisation. A large number of random draws from the probability density function results in a large set of realisations of the sea surface, which is called ensemble.

The variance density spectrum is more meaningful than the amplitude spectrum for two reasons. Firstly, the variance is more useful than amplitude in statistics. For example, the sum of the variances of the wave components is equal to the variance of the sum of the wave components. However, this property is not true for amplitude. Secondly, linear wave theory implies that the energy of the waves is proportional to the variance. This implies that, through the variance, a link is available to such physical properties as wave energy, but also wave-induced particle velocity and pressure variations.

The variance density spectrum $S(f)$, which is continuous, can be transformed from the amplitude spectrum $E\{\underline{a}_i\}$:

$$S(f) = \lim_{\triangle f \to 0} \frac{1}{\Delta f} E\{\frac{1}{2}\underline{a}_i^2\}, \tag{2.16}$$

where Δf is the interval between the frequencies. The variance density spectrum is one of the most important concepts. It gives a complete description of the surface elevation of ocean waves in a statistical sense, provided that the surface elevation can be seen as a stationary, Gaussian process. This implies that all statistical characteristics of the wave field can be expressed in terms of this spectrum. According to the equation of energy in linear wave theory (introduced in §2.2), the energy is associated with the variance of the surface elevation. Therefore, the energy density spectrum can be obtained by multiplying the variance density spectrum $S(f)$ by the gravitational acceleration g and density of water ρ:

$$E_{\text{energy}}(f) = \rho g S(f). \tag{2.17}$$

2.2 Linear wave theory

2.2.1 Hydrodynamic problem

Linear wave theory, as developed by Airy (1845), describes ocean waves by assuming the ocean waves as the sum of lots of independent harmonic waves. In order to develop the linear wave theory for surface gravity waves, water is regarded as an ideal fluid, which is incompressible, irrotational, continuous, constant density, and has no viscosity. The equations in the linear wave theory are based on two balance equations: the mass balance equation and momentum balance equation. In addition, two boundary conditions are also used in the equations derivation. These are the kinematic boundary condition and dynamic boundary condition. The kinematic boundary condition defines that the particles can neither move above the water surface nor pass through the base. Thus, at the water surface, the vertical velocity of the water particle (u_z) should be equal to the speed of surface in the vertical z direction. At the bottom ($z = -d$, d is the water depth), the vertical velocity of the water particle should be zero (For variable depth, the velocity normal to the slope is zero). Therefore,

$$u_z = \frac{\partial \eta}{\partial t} \quad \text{at } z = 0, \tag{2.18}$$

$$u_z = 0 \quad \text{at } z = -d. \tag{2.19}$$

In addition, the dynamic boundary condition defines that the pressure (p) at the water surface ($z = 0$) should be 0 ("zero pressure" is only for gauge pressure and the pressure at the surface should be atmospheric):

$$p = 0 \quad \text{at } z = 0. \tag{2.20}$$

The velocity on each spatial direction can be expressed by the velocity potential function $\phi = \phi(x, y, z, t)$, where the spatial derivative of the velocity potential on each direction is equal to the velocity of the water particle:

$$u_x = \frac{\partial \phi}{\partial x}, \quad u_y = \frac{\partial \phi}{\partial y}, \quad \text{and} \quad u_z = \frac{\partial \phi}{\partial z}. \tag{2.21}$$

The Laplace equation can be obtained from the mass balance equation with the function of ϕ, and it is given by:

$$\frac{\partial^2 \phi}{\partial x^2} + \frac{\partial^2 \phi}{\partial y^2} + \frac{\partial^2 \phi}{\partial z^2} = 0. \tag{2.22}$$

The kinematic and dynamic boundary conditions can provide a particular solution to the Laplace equation. The Bernoulli equation can be obtained from the momentum balance equation with the function of ϕ, and it is given by:

$$\frac{\partial \phi}{\partial t} + \frac{p}{\rho} + gz = 0. \tag{2.23}$$

The dynamic boundary condition is an application of Bernoulli equation at the free surface. Except for the kinematic and dynamic boundary conditions, fully reflective boundary condition should be considered when waves hit the sidewall of the domain. The reflected wave should be the same as the incident wave in terms of amplitude and only the propagation direction is changed.

2.2.2 Kinematics

Based on the expression of the velocity potential function (Dean and Dalrymple, 1991),

$$\phi = \frac{\omega a}{k} \frac{\cosh[k(d+z)]}{\sinh(kd)} \cos(\omega t - kx), \tag{2.24}$$

the particle velocity can be derived by calculating the spatial derivative giving:

$$u_x = \frac{\partial \phi}{\partial x} = \omega a \frac{\cosh[k(d+z)]}{\sinh(kd)} \sin(\omega t - kx), \tag{2.25}$$

$$u_z = \frac{\partial \phi}{\partial z} = \omega a \frac{\sinh[k(d+z)]}{\sinh(kd)} \cos(\omega t - kx), \tag{2.26}$$

where a is the wave amplitude, u_x and u_z are horizontal velocity and vertical velocity, respectively, ω is the angular frequency, and k is the wave number, d is the water depth, and z indicates the location on the vertical coordinate.

The movement of the water particles is circular or elliptical in deep and finite depth water respectively. Therefore, these velocities are also known as orbital velocities. In deep water, kd can be regarded as infinity, and the magnitude of the resultant velocity is $\omega a e^{kz}$. Based on the expression of resultant velocity in deep water, it shows the particle velocity become smaller in the deeper-water depth ($z < 0$), and the max value occurs on the surface ($z = 0$), which is equal to ωa. By contrast, when it comes to the shallow water, where kd approaches 0, the expression shows that the horizontal velocity is independent of the water depth(z).

2.2.3 Dynamics

A unidirectional linear regular wave travelling in the x-direction with a single frequency can be expressed by amplitude a, frequency ω, and wavenumber k. The surface elevation $\eta(x,t)$ at specific time t, and spatial position x is given by:

$$\eta(x,t) = a\cos(\omega t - kx). \tag{2.27}$$

In terms of the free wave, the frequency ω and wave number k are related by the dispersion relationship:

$$\omega^2 = gk \tanh(kd). \tag{2.28}$$

In deep water, the water depth $kd \to \infty$ and $\tanh(kd) \to 1$. In shallower water, the water depth d $kd \to 0$ and $\tanh(kd) \to kd$. Then, the dispersion relationship is given by:

$$\omega = \sqrt{gk} \quad \text{for} \quad \text{deep} \quad \text{water}, \tag{2.29}$$

$$\omega = k\sqrt{gd} \quad \text{for} \quad \text{shallow} \quad \text{water}. \tag{2.30}$$

2.2.4 Wave energy

Wave energy can be divided into potential energy, due to the particle location and gravity, and kinetic energy, due to the particle motion. Based on Holthuijsen (2010), the potential and kinetic energy per unit horizontal area are given by:

$$E_{\text{potential}} = \frac{1}{4}\rho g a^2, \tag{2.31}$$

$$E_{\text{kinetic}} = \frac{1}{4}\rho g a^2. \tag{2.32}$$

where a is the wave amplitude of the harmonic wave. ρ and g are fluid density and gravitational acceleration respectively. The energies are averaged over a wavelength. Based on the expression, in linear wave theory, the potential energy and kinetic energy are equal in magnitude, and the total energy is equal to the sum of the two.

When it comes to the energy of wave groups, the potential energy can be calculated

by integrating the surface elevation square (η^2) over the fluid surface (s) (Gibbs, 2004). The kinetic energy can be calculated by integrating the product of the time derivatives of surface elevation (η_t) and the velocity potential at a specific spatial location (ϕ^s) over the fluid surface. Therefore,

$$E_{\text{potential}} = \frac{1}{2}\rho g \int \int \eta^2 \mathrm{d}s, \tag{2.33}$$

$$E_{\text{kinetic}} = \frac{1}{2}\rho \int \int \phi^s \eta_t \mathrm{d}s. \tag{2.34}$$

2.3 Wave propagating on a variable bathymetry

One of the mechanisms which causes the rogue waves is wave propagation over abrupt depth transitions, which is examined in this section.

2.3.1 Waves over gentle changes in bathymetry (linear shoaling)

Linear shoaling cannot provoke the rogue waves. However, we first introduce linear shoaling here to provide the basic information of wave parameters when a wave propagates over a slope.

A harmonic wave retains its frequency when it propagates over a gentle slope. Based on the dispersion relationship, its wave length will decrease. As the depth decreases, the phase speed will correspondingly decrease:

$$c = \sqrt{\frac{g}{k}\tanh(kd)}, \tag{2.35}$$

in which c is the phase speed and k is the wavenumber. g is the acceleration of gravity and d is the water depth. With the depth decrease, the group velocity c_g increases

slightly, but then decreases as the water depth gets shallower:

$$c_g = nc \quad \text{with} \quad n = \frac{1}{2}\left(1 + \frac{2kd}{\sinh(2kd)}\right). \tag{2.36}$$

When waves propagate from deeper-water to shallower-water side, the phase speed approaches the group speed, and the waves becomes less and less dispersive as phase speed is less dependent on the frequency. Finally, both the phase speed and the group speed approach zero at the waterline, although linear theory will have broken down before that point.

The variations of the group speed can cause the variations of local wave energy and the amplitude. To understand these variations, we can consider a simple model with wave propagating through shallow water towards a straight coastline at normal incidence under stationary conditions (no variations occur along the wave crest and hence no refraction). If we have two vertical planes, plane 1 and plane 2, which are located at seaward side (deeper-water side) and beachward side (shallower-water side), respectively. Under such conditions, in the absence of any energy generation or dissipation, wave energy can only enter through plane 1 and leave through plane 2. Based on the conservation of energy, the wave amplitude on the shallower-water side can be obtained from:

$$P_2 b = P_1 b \rightarrow [Ec_g]_2 = [Ec_g]_1 \rightarrow \frac{1}{2}\rho g a_2^2 c_{g,2} = \frac{1}{2}\rho g a_1^2 c_{g,1}, \tag{2.37}$$

in which P_1 and P_2 are wave energy flux at plane 1 and plane 2, a_1 and a_2 are wave amplitude at plane 1 and plane 2, ρ is the density and g is acceleration of gravity. The wave amplitude on shallower-water side is given by:

$$a_2 = \sqrt{\frac{c_{g,1}}{c_{g,2}}} a_1, \tag{2.38}$$

The shoaling effect can lead to the slightly decrease but then to an increase of

the wave amplitude along the propagation. As the group velocity approaches to zero at the waterline, the wave amplitude theoretically goes to infinity. However, the evolution of the waves can also be determined by other processes, such as wave breaking, which results in a totally different evolution.

2.3.2 Statistical deviations from Gaussian model

The statistical distribution of waves can be modified by the change of depth. This was investigated in the pioneering work of Bitner (1980), who reported an experiment of waves propagating towards decreasing depth. When a wave is propagating on a decreasing depth, inconsistencies are found between experiments and a Gaussian distribution base on this study. The probability density functions of wave heights, wave phases and phase velocities, the distribution of wave-lengths, mean wave height and mean wave-length were given. Kurtosis and skewness are used to describe how nonlinear the waves are. Skewness describes the asymmetry of the probability distribution. Kurtosis implies the probability of extreme events. The magnitudes of kurtosis and skewness, depending on the phase of transformation of waves, are found to have the maximum value at the plunging breaker line (Bitner, 1980). The skewness μ_3 and kurtosis μ_4 can be calculated by surface elevation η_i, the time mean value of surface elevation η_{mn} and the root mean square value of surface elevation η_{rms}:

$$\mu_3 = \frac{1}{\eta_{rms}^3}\frac{1}{n}\sum_{i=1}^{n}(\eta_i - \eta_{mn})^3, \tag{2.39}$$

$$\mu_4 = \frac{1}{\eta_{rms}^4}\frac{1}{n}\sum_{i=1}^{n}(\eta_i - \eta_{mn})^4. \tag{2.40}$$

2.3.3 Wave propagation over a bar

The work of Grue (1992) focused on the nonlinear diffraction of low-amplitude gravity waves in deep water due to a slightly submerged obstacle, which is cylindrical or rectangular in the bottom topography. It is found that strong nonlinear deformations occur to the incoming waves at the location of the obstacle, inducing a large number of super-harmonic waves mainly at the lee side of the obstacle. The amplitudes of the super-harmonic waves are proportional to the amplitudes of the incoming waves, and the amplitudes of some super-harmonic waves are even large enough to be comparable with the amplitudes of the incoming waves, implying that linear theory has completely broken down. Wave propagation over a bar is also studied by Beji and Battjes (1993). It is found high frequency energy generation can be observed based on the wave spectrum of the experimental waves when waves propagate over a bar, which contributes to amplification of the bound harmonics waves.

2.3.4 Evidence for the rogue waves at the top of an abrupt depth transition

Numerous results of numerical simulations and experimental data have shown a significant dynamic response that occurs after the depth change (Sergeeva et al., 2011; Trulsen et al., 2012; Zeng and Trulsen, 2012; Gramstad et al., 2013; Kashima et al., 2014; Viotti and Dias, 2014; Bolles et al., 2019; Zhang et al., 2019). Kurtosis and skewness are mainly used as proxy parameters to describe how strong the wave nonlinearities.

Evidence of the rogue waves in experiments

Rogue wave statistics of waves over a shoal were studied by Trulsen et al. (2020). Kurtosis and skewness are indicators of deviation from a linear model of wave statistics.

Trulsen et al. (2020) investigated the statistics of surface elevation and horizontal fluid velocity when waves propagated over a shoal, and the experiment was carried out at the Hydrodynamical Laboratory of the Department of Mathematics at the University of Oslo. Their paper found that the surface elevation has a local maximum of skewness and kurtosis above the shallower part of the shoal close to the edge on the incoming side. The local minimum of skewness occurs on the downward slope on the lee side of the shoal. In terms of the horizontal velocity, it is found the local maximum and minimum of skewness occur at the same locations as those of the surface elevation. However, the local maximum of the kurtosis occurs over the downward slope on the lee side of the shoal.

In the experiments of Trulsen et al. (2012), a local maximum of kurtosis and skewness can occur on the shallower-water side of the slope, when unidirectional waves propagate over a sloping bottom. Furthermore, the probability of large waves also has a local maximum near the top of the slope. Therefore, the anticipated probability of a rogue wave could also have a local maximum near the shallower-water side of a slope.

Similar investigation is carried out by Bolles et al. (2019), studying the wave propagation over a step in an experimental wave tank. They found that abrupt depth change in the bottom topography can qualitatively change the distribution of the surface waves. A normally distributed wave field can be highly skewed and the distribution starts to deviate from the Gaussian distribution after the abrupt depth change. It is also found that in a short distance downstream after the step, the wave statistics follow a Gamma distribution, and we can use Gamma distribution to roughly estimate the statistical properties, such as kurtosis and skewness. The Gamma distribution of the surface elevation is given by:

$$p(\eta) = \frac{e^{-\alpha}}{\eta_\gamma \Gamma(\alpha)} \left(\alpha + \frac{\eta}{\eta_\gamma}\right)^{\alpha-1} \exp\left(\frac{-\eta}{\eta_\gamma}\right), \tag{2.41}$$

in which η_γ and α are the scale and shape parameters, respectively (Bolles et al., 2019).

Other researchers also have similar conclusions on this problem. Zhang et al. (2019) found that the higher probability of the occurrence of the rogue waves is found in their experiments and the local maximum values of skewness and kurtosis are observed around the end of the depth change. According to the experimental results of Kashima et al. (2014), it is shown that the maximum wave heights increases with an increase in kurtosis.

Evidence of the rogue waves in numerical simulations

Numerical simulations have been widely conducted to investigate the influence of the depth transition on waves statistics. The Korteweg-de Vries equation was used by Sergeeva et al. (2011) to analyse the transformation of the waves on the shallow water side of the depth transition. They found the skewness and kurtosis increase as water depth decreases. At the same time, the wave state starts to depart from the Gaussian, and the probability of the rogue waves increases in the transition zone. According to the numerical results, there is a significant increase of the total number of the rogue waves compared with the values derived from the case with flat bottom of a given depth.

Similar results are also found by Gramstad et al. (2013), in which a Boussinesq model with improved linear dispersion was used. The numerical evidence also shows that the depth transition can provoke a considerable increase of the probability of the rogue waves. The skewness, kurtosis and probability of the rogue waves increase on the shallower side of a slope, and reach a maximum value near the top of the slope. In addition, the increased probability of the rogue waves is maintained for some distance on the shallower-water side, before it decreases and reaches a stable value.

The study of Viotti and Dias (2014) showed that the rogue waves can be triggered

by strong depth change when surface gravity waves propagate over uneven bathymetries, which was studied by means of spectral simulations of the free-surface Euler equations. The strong non-Gaussian statistics are observed in a region around the step. After this, statistical properties settle rapidly on the steady statistical state of finite-depth random wave fields. Extreme fluctuations are enhanced by strong depth transitions, leading to the formation of the rogue waves.

Evidence in the field data

Cherneva et al. (2005) analysed the field data gathered in the coastal zone of the Bulgarian part of the Black sea with depth decreasing from 18 m to 1.3 m. In a linear model of wave propagation, the free surface is typically modelled as Gaussian distributed with the crest statistics approximately following the Rayleigh distribution (Longuet-Higgins, 1952). However, it is found when waves propagate on a gentle decreasing depth, there is a significant deviation from the Gaussian distribution. Cherneva et al. (2005) found that the probabilities of the large waves are always underestimated by all theories, including the second-order model of Ochi (Ochi and Wang, 1985), the second-order model of Al-Humoud, Tayfun and Askar (Al-Humoud et al., 2002) and the model of Mori and Yasuda (Mori and Yasuda, 2002). The probability distribution of peaks, troughs and heights are still not accurate enough to evaluate the real waves in the ocean, although these three models, considering different statistical parameters, have their own advantages, and can still be used for some specific problems. Some other field data can also show that the rogue waves can be trigger by depth transition in the bottom topography (Didenkulova and Anderson, 2010; Didenkulova, 2011).

2.3.5 Theories to explain the influence of the depth transition

There are two suggested mechanisms to explain the formation of the rogue waves triggered by the depth transition. Li et al. (2021c) derive a second-order theory for surface gravity wave groups propagating over an abrupt depth transition. In addition, experiments for waves propagation over an abrupt depth transition are carried out to validate the theory (Li et al., 2021a). Based on the results, it is found that the magnitude of the second-order bound waves changes, and free wave groups are released when the main wave group reaches the step. Free second-order super-harmonic waves and second-order sub-harmonics waves propagate at different speeds compared with the main wave group, leading to the local behaviour at the top of the depth transition such as local superposition and the corresponding overall maximum crest amplitude. In addition, this second-order theory suggests that the magnitude of the maximum crest can be 1.75 times larger than that of the linear focused wave crest, leading to a considerable increase of skewness. Thus, the vertically skewed surface elevation and the considerable increase of the wave amplitude can explain the local change in wave statistics near the top of the depth transition.

The second suggested mechanism is based on the idea of spectral equilibrium (see Barratt et al. (2022) and papers cited therein). When the boundary conditions imposed on a sea-state suddenly change, as would happen as it passes over a depth discontinuity, the wave spectrum needs to adjust to regain balance between the non-linear terms. The non-linear physics can lead to rogue waves although the detailed mechanisms are not well understood. Zeng and Trulsen (2012); Viotti and Dias (2014) have proposed this as a mechanism which can lead to extreme waves at the top of depth discontinuities.

2.3.6 Changes to the shape of average extreme events

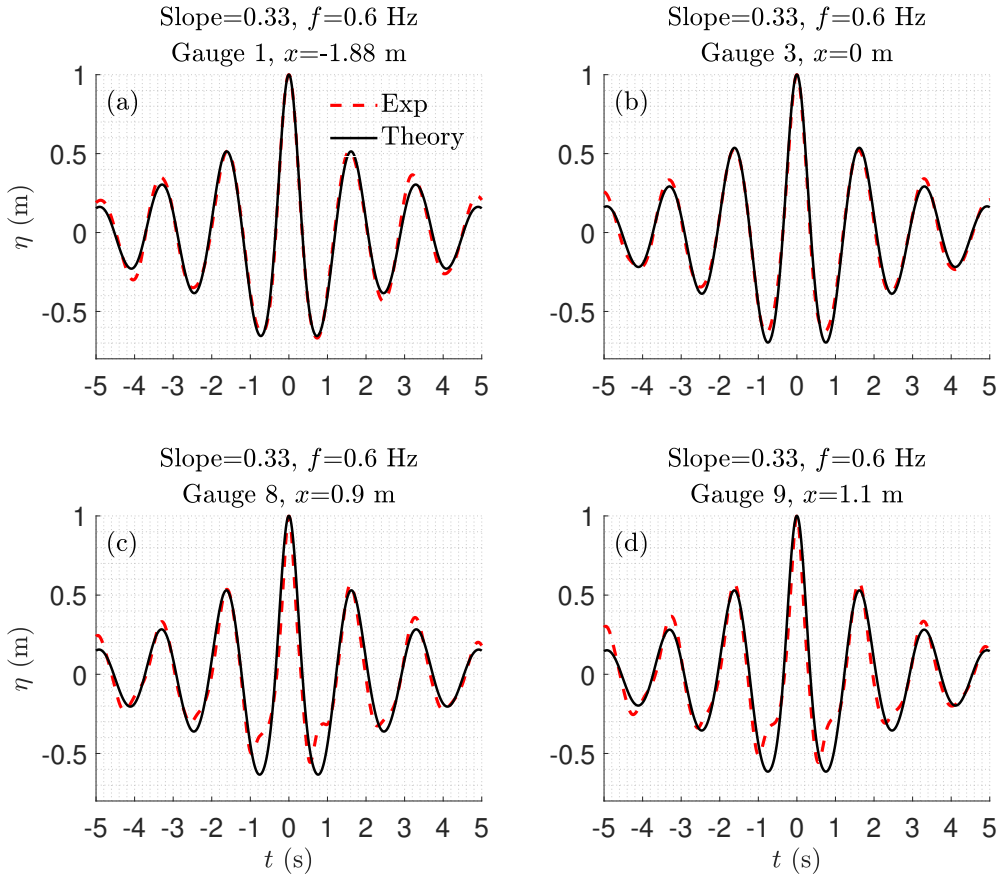


Figure 2.1: Comparison between experimental and theoretical average shape of extreme events at different locations. x indicates the distance to the top of the slope, and positive value means location after the slope. t is time, and η is the surface elevation, f is the peak frequency, and Slope is the gradient of the seabed slope.

If the time series is assumed to follow the linear model, the theoretical expected shape of the extreme events can be evaluated by 'NewWave' (Lindgren et al., 1970; Boccotti, 1983; Tromans et al., 1991):

$$\eta(t) = \frac{1}{m_0} \int_0^\infty E(f) \cos(2\pi f t) \mathrm{d}f, \tag{2.42}$$

in which $E(f)$ is the spectrum, and m_0 is the zeroth-order moment of the spectrum. f is frequency, and t is time. $\eta(t)$ indicates the NewWave profile.

In Figure 2.1, we examine the average shape of the largest events of experimental data from Li et al. (2021a), and the theoretical shape is calculated by equation (2.42). In Figure 2.1, x indicates the distance to the top of the slope, and a positive number is corresponding to location after the slope. We can find that the average shape of extreme events of the experimental data deviates a lot from the theoretical shape after the top of the slope.

2.4 Wave loading on cylinders

Tubular mechanical components are common for offshore structures. The life span of the structures is related to the material strength and the effect of fatigue. Therefore, wave loading on the structure needs to be understood to evaluate the life span of the structures.

Offshore structures are divided into categories based on their diameter. A large diameter cylinder is defined when the ratio between the diameter and the wave-length is bigger than 0.2 ($D/\lambda > 0.2$). In this case, the incident wave pattern is influenced, leading to diffraction and wave scattering. The inertial force is mainly considered, which is caused by the acceleration of the flow, and viscous effects are negligible. In terms of the small diameter cylinders, in which the ratio between the diameter and the wave-length is smaller than 0.2 ($D/\lambda < 0.2$), there is only relatively small impact on the wave pattern. The loading has both inertial and drag components, caused by formation of the wake behind the cylinder.

Morison equation is used to calculate the force on the fixed vertical cylinder as the sum of drag and inertial components (Morison et al., 1950):

$$f_I = \frac{1}{2}\rho D C_D u|u| + \rho\frac{\pi D^2}{4} C_M \frac{du}{dt}, \tag{2.43}$$

in which ρ is the water density, D the diameter of the cylinder, u the instantaneous

horizontal particle velocity, C_D the drag coefficient and C_M the inertial coefficient. The first term describes the drag force, which forms due to the boundary layer separation and wake effects. Reynolds number is the determinate criterion to decide the type of drag force, including skin friction drag and pressure drag, which dominate when Reynolds number (Re) is low and when Re>100, respectively. The second term, the inertial force, is evaluated using the relative acceleration between cylinder and flow. There are also two components in the inertial force, which includes Froude-Krylov force because of the pressure gradient in the flow and added-mass force caused by local disturbance to the flow.

2.5 Introduction to OceanWave3D

This project uses OceanWave3D to solve fully non-linear potential-flow water-wave equations. This code is chosen because of its ability to handle depth discontinuities, and because of existing expertise in the Oxford group. OceanWave3D can be downloaded online. We use the version of 2020 and we believe that our simulation results can be reproduced by any version of OceanWave3D.

2.5.1 Code description

OceanWave3D (OW3D) is a fully nonlinear potential-flow solver (Engsig-Karup et al., 2009). In OW3D, the nonlinear terms of the free-surface boundary conditions are included during the time marching of the initial conditions. Potential-flow equations for surface gravity waves are solved by OW3D in a three-dimensional Eulerian framework (Engsig-Karup et al., 2009). In addition, a Cartesian coordinate system (x, y, z) is adopted in this Eulerian frame, with the xy-plane located at the still water level, and the positive direction of the z-axis pointing upwards. In the simulation, nodes on the x-axis and y-axis are uniformly distributed. However, N_z, the total number of nodes

on the z-axis, is defined in OW3D, and the nodes are unevenly distributed. The vertical distance between the free surface and the bottom is always changing with time as wave propagationes. Therefore, it is convenient to map the solutions to a time-invariant domain, and σ-coordinate is used in numerical simulation (Engsig-Karup et al., 2009).

Classical fourth-order Runge-Kutta time marching is applied in OW3D. A nonlinear matrix and preconditioning matrix are constructed by OW3D during the numerical simulation. Central differencing is applied for both matrices, and the order of convergence for finite difference schemes is also defined for these two matrices. However, central differencing is not applied at the boundaries of the numerical domain because of lack of sufficient nodes outside of the boundaries. The order of finite differencing is consistent for the entire numerical domain. Ghost nodes are defined outside the numerical domain for all surfaces except the free surface. The ghost nodes at the bottom boundary make sure of continuity and increase the numerical stability of the preconditioning scheme. For nodes on the z-axis, in which nodes are unevenly distributed, ghost points can also be used and increase the numerical stability.

The nonlinear matrix is used for data storing and solved by generalised minimum residual (GMRES) algorithm, which is extremely robust but memory intensive. At each time step of the numerical simulation, we define a relative tolerance (for example, 10^{-6}) for the convergence of the GMRES algorithm to make sure the simulation is both accurate and efficient. Preconditioning of the nonlinear matrix can minimise the number of iterations at each time step and expedite the solution procedure, which is performed by evaluating a preconditioning matrix. Preconditioning is always performed once in each iteration with the multi-grid method. The multi-grid scheme follows the direct coarse grid approximation, and V-cycle is used for multi-grid scheme. The grid descends from the finest grid resolution down to the coarsest grid resolution at first. Then it ascends from the coarsest grid resolution to the finest grid

resolution and always follows this loop. Multi-grid method accelerates the iterative convergence by iterating from finest to coarsest of the grid at each time step.

2.5.2 Formulation of the problem

OceanWave3D solves the potential-flow equations, which is introduced in §2.2. The fluid velocity (u,v,w) can be calculated by the gradient of a scalar velocity potential $\phi(x, y, z, t)$

$$(u, v, w) = (\nabla\phi, \partial_z\phi), \tag{2.44}$$

in which $\nabla = (\partial_x, \partial_y)$ is the horizontal gradient operator. Based on the equations established by Zakharov (1968), the kinematic and dynamic free surface boundary conditions can be expressed by using the chain rule on the nonlinear version of Bernoulli equation and nonlinear kinematic boundary condition:

$$\partial_t\eta = -\nabla\eta\cdot\nabla\widetilde{\phi} + \widetilde{w}(1+\nabla\eta\cdot\nabla\eta), \tag{2.45}$$

$$\partial_t\widetilde{\phi} = -g\eta - \frac{1}{2}(\nabla\widetilde{\phi}\cdot\nabla\widetilde{\phi} - \widetilde{w}^2(1+\nabla\eta\cdot\nabla\eta)), \tag{2.46}$$

in which $\widetilde{\phi} = \phi(x, y, \eta, t)$ is the velocity potential at the free surface ($z = \eta$), and $\widetilde{w} = \partial_z\phi|_{z=\eta}$ is the vertical velocity at the free surface. In order to obtain the exact value of the vertical velocity at a specific time, the Laplace equation in the fluid volume is solved, together with the kinematic and dynamic boundary conditions.

As the wave propagates, the free surface, as one of the boundaries, is always changing with time. Therefore, we can map the vertical solutions to a time-invariant domain, and σ-coordinate transformation is used here to achieve the transformation.

$$\sigma = \frac{z + h(x, y)}{\eta(x, y, t) + h(x, y)} = \frac{z + h(x, y)}{d(x, y, t)}. \tag{2.47}$$

$d(x, y, t)$ indicates the vertical distance from the fluid bottom to the free surface. The maximum value of z is equal to $\eta(x, y, t)$, and the minimum value is equal to $-h(x, y)$. In addition, the distribution of nodes in the vertical direction follows the symmetric half of a Chebyshev-Gauss-Lobatto (CGL) distribution (Barratt et al., 2021).

$$\sigma_j = \sin((\pi[j-1])/(2[N_z-1])), \tag{2.48}$$

in which j indicates the index of the nodes in the vertical direction. In addition, j=1 is corresponding to the bottom, and j=N_z is corresponding to the free surface.

After the transformation, the value of σ is on the scale of 0 to 1. In the σ-coordinate, $\mathbf{\Phi}(x, y, \sigma, t) = \phi(x, y, z, t)$, and the Laplace equation is given by:

$$\mathbf{\Phi} = \widetilde{\phi}, \quad \sigma = 1, \tag{2.49}$$

$$\nabla^2\mathbf{\Phi} + \nabla^2\sigma(\partial_\sigma\mathbf{\Phi}) + 2\,\nabla\,\sigma\cdot\nabla(\partial_\sigma\mathbf{\Phi})) + (\nabla\sigma\cdot\nabla\sigma + (\partial_z\sigma)^2)\partial_{\sigma\sigma}\mathbf{\Phi} = 0, \tag{2.50}$$

$$(\partial_z\sigma + \nabla h\cdot\nabla\sigma)(\partial_\sigma\mathbf{\Phi}) + \nabla h\cdot\nabla\mathbf{\Phi} = 0, \quad \sigma = 0. \tag{2.51}$$

After solving the Laplace equation, the vertical velocity $\widetilde{w}$ and velocity potential $\widetilde{\phi}$ can be obtained, which allow the equations (2.45) and (2.46) to be stepped forward in the time domain.

2.5.3 Wave generation and absorption

A Cartesian coordinate system is applied in OceanWave3D, with origin on the still water plane and the z-axis pointing vertically upwards. $\mathbf{x} = [x, y]$ is a horizontal

vector, and t is time. The boundary of the fluid domain is at the sea bottom ($z = -h(\mathbf{x})$) and the free surface ($z = \eta(\mathbf{x}, t)$). The kinematic and dynamic free surface boundary conditions in terms of velocity potential and the vertical component of velocity evaluated on the free surface: $\tilde{\phi} = \phi(\mathbf{x}, \eta, t)$, and $\tilde{w} = \frac{\partial \phi}{\partial z}\big|_{z=\eta}$

$$\eta_t = -\nabla\eta \cdot \nabla\tilde{\phi} + \tilde{w}(1 + \nabla\eta \cdot \nabla\eta), \tag{2.52}$$

$$\tilde{\phi}_t = -g\eta - \frac{1}{2}\nabla\tilde{\phi} \cdot \nabla\tilde{\phi} + \frac{1}{2}\tilde{w}^2(1 + \nabla\eta \cdot \nabla\eta) - p_D. \tag{2.53}$$

in which $\nabla = [\partial/\partial x, \partial/\partial y]$ is the horizontal gradient operator, and g is the gravitational acceleration. p_D is damping pressure, and it is used as wave absorption in the simulation. OceanWave3D allows velocity damping and pressure damping. In our simulations of OceanWave3D, we only use pressure damping for wave absorption. Thus, in order to avoid misleading, we only present the equation for pressure damping.

The method of damping waves in the numerical simulation is similar to the linear friction damping in the mechanical system, and the method is given by:

$$p_D = \gamma\widetilde{\phi}, \tag{2.54}$$

in which γ is a spatially varying function, and it defines the damping zone. The value should be zero if no damping is imposed. However, Clamond et al. (2005) find that the above friction damping applied to the velocity potential is not a pure damping term but it also generates waves. It is not efficient enough to apply just friction damping to a physical velocity variable. Thus they get the damping term by using the dynamic free surface boundary condition and integrating the equation, which is the method in OceanWave3D. $B(t)$ is the Bernoulli constant.

$$p_D = \nabla^{-1} \cdot (\gamma \nabla \widetilde{\phi}) - B(t). \tag{2.55}$$

Relaxation of the numerical solution to a specified analytic solution over a region of the numerical domain can also be used as wave generation and absorption. This method is often used in ocean circulation modelling (Jensen, 1998). Such a relaxation zone is readily achieved by simply defining a relaxation coefficient $0 \leq c_r(\mathbf{x}) \leq 1$, and an exact desired solution $\left(\eta^e, \tilde{\phi}^e\right)$. After each stage of time integration the solution within the relaxation zone is then redefined to be:

$$\eta(x,t) = [1 - c_r(x)]\eta(x,t) + c_r(x)\eta^e(x,t), \tag{2.56}$$

$$\widetilde{\phi}(x,t) = [1 - c_r(x)]\widetilde{\phi}(x,t) + c_r(x)\widetilde{\phi}^e(x,t). \tag{2.57}$$

Chapter 3

On Rogue Waves Generated by Abrupt Depth Transitions

3.1 Abstract

Wave propagation over variable bathymetry is known as one of the possible mechanisms that can provoke rogue waves. In this paper, we use a fully nonlinear potential-flow solver, OceanWave3D, to simulate the process of waves propagating over variable bathymetry and analyse the kinematics under the free surface near the top of the slope. To achieve this, we first evaluate the accuracy of the numerical results generated by OceanWave3D. We carry out convergence tests to examine the influence of different parameters in OceanWave3D on the numerical results. Based on verification and validation tests, we evaluate the accuracy of OceanWave3D for problems with variable bathymetry comparing numerical and experimental results. We find that OceanWave3D is accurate enough to solve equations for problems with abrupt depth transitions and the agreement between experimental results and numerical results is good. Finally, we investigate the kinematics and we find that a slope can not only amplify crest amplitudes but also increase the wave kinematics near the top of the

slope, which has obvious implications for loads on offshore structures.

3.2 Introduction

Large ocean waves are of interest to scientists and engineers. In particular there is interest in what can cause larger waves than predicted by linear wave dynamics. Various mechanisms have been proposed which might give rise to such so called rogue or freak waves (Kharif and Pelinovsky, 2003; Dysthe et al., 2008; Onorato et al., 2013; Adcock and Taylor, 2014). One which has received considerable attention over the past decade is where waves pass over abrupt depth transitions (Sergeeva et al., 2011; Trulsen et al., 2012; Gramstad et al., 2013; Bolles et al., 2019; Zheng et al., 2020). Li et al. (2021c) argue that the release of bound components as the water depth changes is the primary cause of the excess number of rogue waves which have been observed in experiments and numerically. Modelling these waves passing over abrupt depth transitions to better understand this phenomenon is the subject of this paper.

Ocean waves are typically modelled using potential flow equations. Numerically solving these equations is a well known problem in ocean engineering and a number of techniques exist. Some, such as Green function codes (Xie et al., 2018) are excellent for solving problems with complex domains but relatively high computational demands. SPH is also an alternative (Draycott et al., 2022) (not solve equations for potential flow). Here we examine whether the numerical model OceanWave3D (OW3D) can be used for modelling waves passing over abrupt changes in bathymetry. Following this we exploit the fact that OW3D explicitly solves for the internal kinematics under the waves to do a preliminary investigation of the impact on the fluid motion of the waves passing over the step.

3.3 Methodology

In this section, the numerical simulation and the experimental set-up are introduced.

3.3.1 Numerical simulations by OW3D

In this paper, all of the numerical results are generated using OW3D (Engsig-Karup et al., 2009). The code time-marches the classical potential-flow water-wave equations. The code has been extensively used for modelling water wave propagation and kinematic (Barratt et al., 2020, 2021). OW3D is a fully nonlinear potential-flow solver (Engsig-Karup et al., 2009). Potential-flow equations for surface gravity waves are solved by OW3D in a three-dimensional Eulerian frame (Engsig-Karup et al., 2009), which gives the kinematics information not only at the free-surface boundary but also at all the vertical nodes hence allowing full kinematic reconstruction. Hence, in this study, the wave kinematics results are extracted directly during the time marching process without any further assumptions. A classical fourth-order Runge-Kutta time marching is applied in OW3D. In OW3D, a σ-coordinate transformation is applied to map the vertical solutions to a time-invariant grid, which can also be used to solve the fully nonlinear potential-flow equations with variable bathymetry. The numerical results from OW3D for nonlinear waves on a semi-circular shoal has been validated against the experiments (Whalin, 1971) in previous studies (Engsig-Karup et al., 2009).

The numerical domain and wave parameters selected vary depending on the particular case considered. Distances in the horizontal are given by x and in the vertical by z with a datum of mean water level. In the convergence tests presented in §3.4.1, the length of the numerical domain, L_x, is fixed as 140 times the wave-length, calculated by peak wavenumber (L_x=30,720 m). The time duration of the simulations is equal to 160 times the wave period, calculated by peak frequency (t=1920 s). The

water depth in the simulation is 500 m (giving non-dimensional depth kh = 14). In terms of the wave parameters, the representative wave-length (λ) is 225 m and the wave period (T) is 12 s.

In the convergence test, the values of Δt, Δx and N_z are changed to investigate the influence of different values. The different values of these three parameters and the corresponding number of nodes per wave-length ($\lambda/\Delta x$) or time steps per wave period ($T/\Delta t$) are given in Table 3.1. λ and T are calculated based on peak wavenumber and peak frequency, respectively. The number of nodes on the x-axis, N_x, varies between 2049 and 4097. This results in a variation in Δx between 15 m (15 points per wave-length) to 7.5 m (30 points per wave-length). The value of Δt, the time interval between two time steps, varies between 0.3 s (40 time steps per wave period) and 0.8 s (15 time steps per wave period). The number of nodes in the vertical direction, N_z, is varied between 20 to 40, which are clustered to give greater resolution near the free surface (see equation (4) in Engsig-Karup et al. (2009)).

Δt $(T/\Delta t)$	Δx $(\lambda/\Delta x)$	N_z
0.30 (40)	7.5 (30)	20
0.34 (35)		
0.40 (30)	12.0 (19)	30
0.48 (25)		
0.60 (20)	15.0 (15)	40
0.80 (15)		

Table 3.1: Different values of Δt, Δx and N_z in OW3D and their corresponding nodes per wave-length ($\lambda/\Delta x$) or time steps per wave period ($T/\Delta t$).

The convergence condition by Courant–Friedrichs–Lewy is a necessary condition for convergence while solving certain partial differential equations numerically. The value of CFL number in the convergence test can be calculated based on the Δx, Δt and group velocity c_g, which is given by:

$$\mathrm{CFL} = \frac{\mathrm{c_g} \cdot \Delta \mathrm{t}}{\Delta \mathrm{x}}, \tag{3.1}$$

In order to demonstrate the variation of CFL number in the convergence test, we calculate the CFL number by using different values of Δt and Δx = 7.5 m, which are shown in Table 3.2.

Δt (s)	Δx (m)	CFL
0.30	7.50	0.375
0.34		0.425
0.40		0.500
0.48		0.600
0.60		0.750
0.80		1.000

Table 3.2: Variation of CFL number in OW3D when using different values of Δt and Δx =7.5 m to calculate the CFL number.

	L_x (m)	N_x	t (s)	Δt (s)
Verification tests	200	32000	120	0.00125
Validation tests	54	3500	64	0.00781

	N_z	kd_s	kd_d	λ (m)
Verification tests	20	0.37	1.03	3.36
Validation tests	20	0.78	1.55	2.23

Table 3.3: Length of the numerical domain L_x, number of nodes on the x-axis N_x, time duration of the simulation t, time interval between two time steps Δt, number of nodes on the z-axis N_z, non-dimensional depth in shallower water kd_s, non-dimensional depth in deeper water kd_d and wave-length λ.

The numerical domain and wave parameters of the verification and validation tests are presented in Table 3.3. In the verification test simulations, the waves are generated and fluxed in from the left boundary of the numerical domain and absorbed on the right. Thus a relaxation zone and a damping zone are used. The relaxation zone is used for generation of the wave in the numerical domain and is located from 0 m to 10 m (3 times the wave-length) on the x-axis. The damping zone, used for wave absorption, is located from 190 m (56.6 times the wave-length) to 200 m (59.6 times the wave-length). The water depth on the deep-water side is 0.55 m (the non-dimensional water depth kh is 1.03) and in shallower-water side is 0.2 m (the

non-dimensional water depth kh is 0.37). Therefore, the water depth change (Δh) is fixed as 0.35 m. Although the gradient of the slope changes for different cases from 0.33 to 14, the top of the slope is always located at x=110 m.

In the validation test, we use two relaxation zones with 'one iteration' for wave generation, similar to Tang and Adcock (2021). The first relaxation zone is located from 0 m to 10 m (4.5 times the wave-length) and the second one is located from 10 m (4.5 times the wave-length) to 20 m (9 times the wave-length). The second relaxation zone is implemented mainly to absorb the reflected wave, caused by the reflection of waves reaching the slope. The location of the damping zone is from 44 m (20 times the wave-length) to 54 m (24 times the wave-length). The gradient of the slope is 1, and it is located from 21.5 m to 21.88 m in the numerical domain. However, in the simulation, the wave just leaving the second relaxation zone is not exactly equal to the target initial condition. Therefore, an iterative method is used to reduce the disagreement between the numerical wave and the initial condition. The iterative method can be performed by finding the difference between the wave just leaving the second relaxation zone and the expected initial condition. Then, we add the difference onto the initial condition and repeat the same simulation again until the wave leaving the relaxation zones agrees with the iterated initial condition.

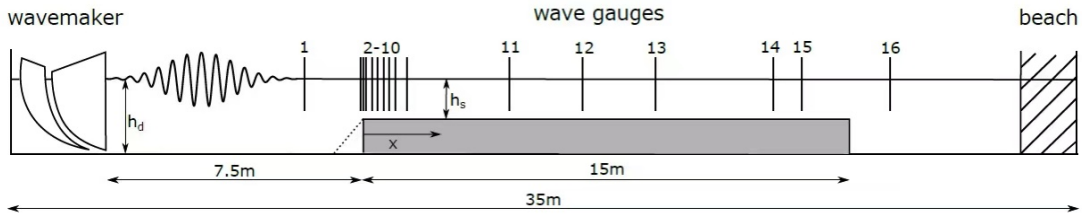


Figure 3.1: Diagram of experimental set-up including gauges, step, beach and wave-maker positions (from Li et al. (2021a)).

3.3.2 Experimental data and set-up

In this paper, all the experimental data are obtained from Li et al. (2021a). The experimental set-up is presented in Figure 3.1. A total of 16 gauges were used to measure the waves of which 4 are selected for comparison with the numerical simulations. Data at gauges 1, 3, 8 and 11 are selected, and the location of these is shown in Table 3.4. The width of the flume is 0.6 m and the length is 35 m. The top of the slope is 7.5 m away from the wave-maker. The water depth of deeper water side, h_d, is 0.55 m and the water depth of shallower water side, h_s, is 0.2 m. Thus the height of the slope is fixed as 0.35 m. The slope is indicated by the dashed line in Figure 3.1, showing a slope of 1:1.

Gauge no.	1	3	8	11
Position x (m)	-1.88	0.00	0.90	5.00

Table 3.4: The locations of gauges 1, 3, 8 and 11 in the experiment. Position x indicates the distance to the top of the slope, and positive value indicates gauges after the top of the slope (from Li et al. (2021a)).

3.4 Verification

Verification is conducted to make sure OW3D is accurately solving the potential-flow equations for wave propagation over steps. However, we start by considering waves propagating over a flat bed. Whilst the accuracy of OW3D is well established for such a case this is helpful in interpreting our later results when varying bathymetry is introduced.

3.4.1 Convergence on flat bathymetry

Simulations of unidirectional waves on a flat bathymetry are run first. We do this to understand the impact of numerical discretisation on the accuracy of the solution We

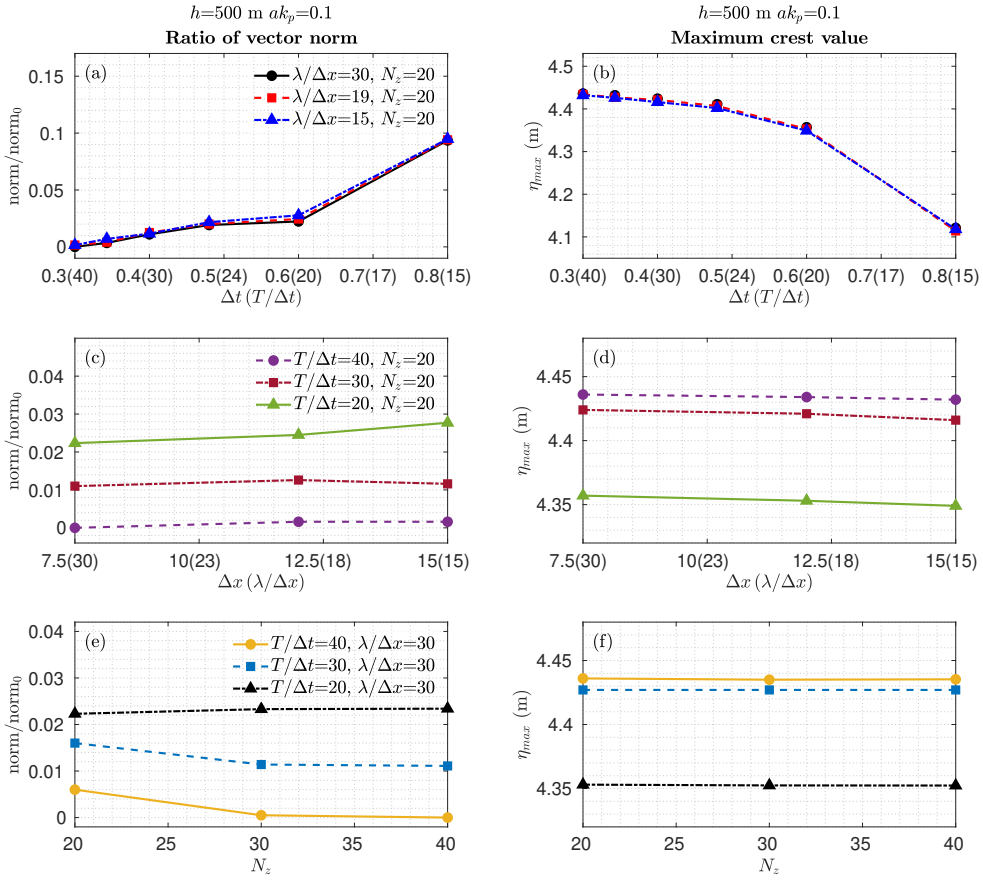


Figure 3.2: Convergence test of different parameters in OW3D for (a, b) Δt, (c, d) Δx, and (e, f) N_z. Parameters are also non-dimensionalised by wave-length (λ) or wave period (T). Δt is the time interval between two time steps. Δx is the spatial interval between two nodes on the x-axis. N_z is the total number of nodes on the z-axis. $T/\Delta t$ is time steps per wave period and $\lambda/\Delta x$ is nodes per wave-length. norm is the vector norm of the difference between the case of interest and the base case. norm_0 is the vector norm of the base case. η_{max} is the maximum surface elevation.

use deterministic wave groups, which we initialise in space using linear theory. The initial wave group is given by wave:

$$\eta(x) = Ae^{-\frac{1}{2}S_x^2 x^2}\cos(k_p x), \tag{3.2}$$

where η is the surface elevation, A is the amplitude, S_x is the spatial bandwidth and it is equal to the spectral width for narrow-banded wave groups and k_p is the peak wavenumber. The velocity potential of the initial condition is also required to be calculated, which can be obtained by linear wave theory. The group propagates for 160 wave periods and at their steepest the waves would have $Ak_p = 0.1$ if the evolution were linear. Note that due to non-linear evolution (e.g. Lo and Mei (1985); Baldock et al. (1996); Adcock and Taylor (2009)) the focus amplitude will be slightly higher than the one predicted by the linear theory. In this case, S_x is 0.004606 m^{-1} which a reasonable value for real ocean waves (Gibbs and Taylor, 2005).

In Figure 3.2, the relationship between the error in the numerical results and the value of different parameters in OW3D is presented. We consider three parameters in OW3D: Δt, Δx and N_z, and show the results in subfigures (a, b), (c, d) and (e, f), respectively. In Figure 3.2, Δt is non-dimensionalised by wave period T and Δx is non-dimensionalised by wave-length λ. λ and T are calculated by peak wavenumber and peak frequency, respectively. The values of Δx, Δt and N_z and their corresponding values of nodes per wave-length ($\lambda/\Delta x$) and time steps per period ($T/\Delta t$) are shown in Table 3.1. It is worth emphasising the most important information is the number of nodes per wave-length or time steps per wave period rather than the absolute values themselves, which ultimately depends on the value of Δt, Δx and N_z in OW3D. In this simulation, the representative wave-length (λ) is 225 m and wave period (T) is 12 s. If the selected parameters in OW3D are Δx=7.5 m and Δt=0.3 s, it means there are approximately 30 nodes per wave-length and 40 steps per period, while solving the potential-flow equations in OW3D.

A base case for the convergence tests is defined with $\lambda/\Delta x$=30, $T/\Delta t$=40 and N_z=20. Different values of Δx and Δt are then considered with the variation being presented in Figure 3.2(a, b), and (c, d). The ratio of the vector norm and the maximum crest values are used to evaluate the difference compared against the base case. L2-vector norm is used in this paper, which is calculated by the square root of the sum of the squared vector values. The vector norm of the difference is defined by the discrepancy between the wave profile of the base case and the wave profile of one of the other cases ($\|(\eta_0 - \eta)\|$). The ratio of the vector norm (norm/norm$_0$) is defined as the ratio between the vector norm of the difference and the vector norm of the wave profile of the base case ($\|(\eta_0)\|$):

$$\text{norm}/\text{norm}_0 = \frac{\|(\eta_0 - \eta)\|}{\|(\eta_0)\|}, \tag{3.3}$$

in which η_0 is the wave profile for the base case in the simulation and η is the wave profile for the case of interest.

Figure 3.2(a, b) shows how the numerical results change with different number of time steps per wave period ($T/\Delta t$). Firstly, the ratio of the vector norm increases and the maximum crest value decreases when decreasing the value of $T/\Delta t$. This means the difference compared with the base case increases, and the accuracy of simulation decreases. Secondly, below value of $T/\Delta t = 20$, there is significant variation in the value of ratio of the vector norm and the maximum crest value. Thus, in the simulations used in this paper a maximum timestep of 1/20 of a wave period is used.

In the convergence test for $\lambda/\Delta x$ and N_z, shown in Figure 3.2(c, d) and (e, f), we can find that there is no significant increase or decrease when changing the value of $\lambda/\Delta x$ or N_z, which means the numerical results are not sensitive to the value of $\lambda/\Delta x$ and N_z for the range of values tested. In each subfigure, there are three lines with different colour and the difference between them is dominated by the different values of $T/\Delta t$. The value of the ratio of between the vector norm and the maximum crest

value shows only little change when changing the value of $\lambda/\Delta x$ or N_z. Thus, there are no limitations, within the range tested, with respect to the value of $\lambda/\Delta x$ and N_z when using OW3D.

3.4.2 Convergence on varying bathymetry

Having examined the propagation of waves on a flat bathymetry in OW3D, we now investigate the accuracy of OW3D when solving potential-flow equations for waves propagating on an abruptly changing bathymetry. To test this, we use the reversibility properties of the governing equations. We run the simulations forward in time up the slope, before reversing the sign of the time step to run the simulations back to the initial conditions. The difference between the initial conditions and the result at the end of the simulations is a rigorous test of numerical accuracy (see Gibbs and Taylor (2005); Barratt et al. (2020)). Similar wave groups to those in the above test are used. In Figure 3.3, the relationship between the gradient of slope and the error in the forward/backward simulations is presented.The gradient of the slope is calculated as the ratio between the water depth change or the height of the slope (Δh) and the horizontal span of the slope(Δd):

$$\text{slope} = \frac{\Delta h}{\Delta d}. \tag{3.4}$$

The water depths are described in §3.3.1, and the size of the horizontal span of the slope is changed, leading to different value of the slope.

To assess the error in the numerical simulation the vector norm is used ($\text{norm}/\text{norm}_0$). It is calculated as the ratio between the vector norm of the difference between the wave group at the start of the forward simulation and the wave group at the end of the backward simulation ($\|(\eta_{\text{forward}} - \eta_{\text{backward}})\|$) and the vector norm of the wave group at the start of the forward case ($\|(\eta_{\text{forward}})\|$):

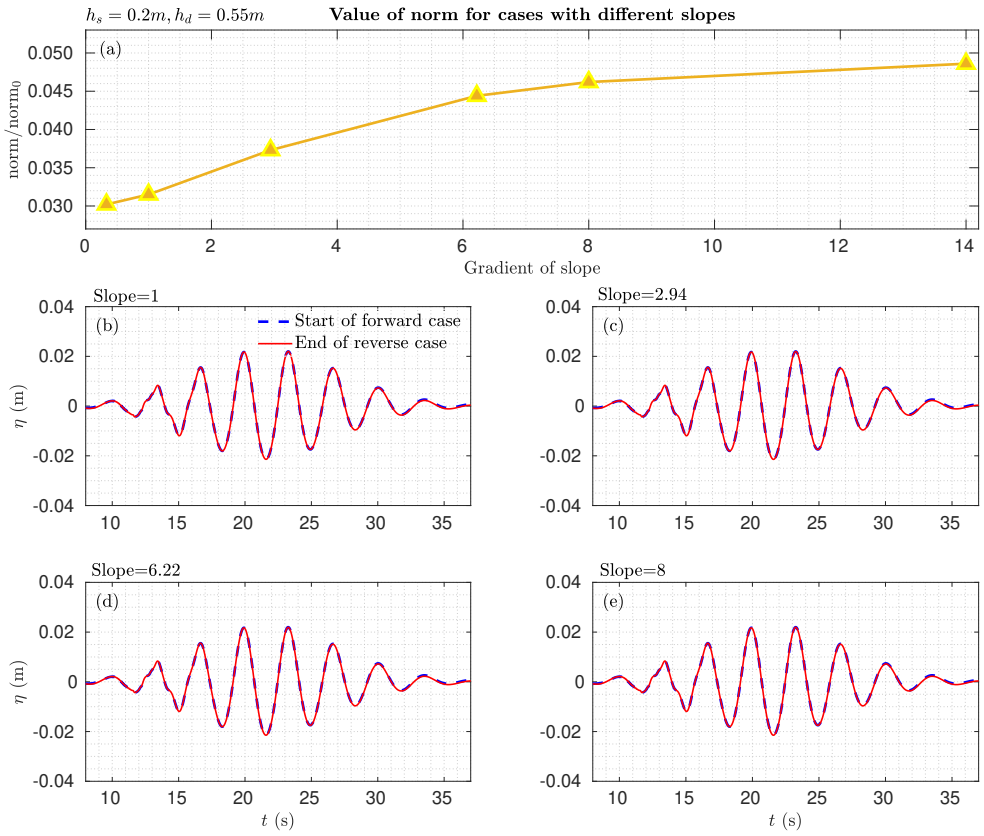


Figure 3.3: Reversibility of OW3D simulation, for (a) the relationship between the gradient of slope and the numerical difference, for (b, c, d, e) the comparison between the wave group at the start of the forward case and at the end of the backward case in different slopes. norm/norm$_0$ is the ratio between the vector norm of difference and the vector norm of the wave group at the start of the forward case; η is the surface elevation and t is time.

$$\text{norm}/\text{norm}_0 = \frac{\|(\eta_{\text{forward}} - \eta_{\text{backward}})\|}{\|(\eta_{\text{forward}})\|}. \tag{3.5}$$

Therefore, if the value of norm/norm$_0$ is smaller, there is less difference between the forward and reverse runs. In Figure 3.3(a), the difference (i.e., norm/norm$_0$)) increases as the slope increases. Thus, the simulation error increases for steeper slopes. However, a plateau is reached for slopes steeper than 6, where the ratio converges to a value around 0.05.

In addition, in Figure 3.3(b, c, d, e), we present the comparisons between the wave group at the start of the forward simulation and the wave group at the end of the backward simulation for different slopes. These subfigures show that the agreement between these two wave group is visually acceptable for all cases. Thus we have confidence that, at the resolution chosen, OW3D can solve the governing equations accurately even when steep slopes are included in the domain.

3.5 Validation: comparison with experimental data

In the verification, we focus on investigating the numerical accuracy when OW3D solves the governing equations. However, in the validation, we focus on investigating whether the OW3D can capture the physics in the real ocean. In our validation, We compare numerical and experimental results to understand the difference between actual waves in the experiment and waves generated by the numerical tank.

In the experiment (see §3.3.2) the wave propagates from deeper to shallow water up a steep slope. The data at probe 1, which is located 1.88 m before the top of the slope, is used as the input to the simulation. The numerical domain and relaxation zones are introduced in Table 3.3 and §3.3.1. The numerical bathymetry is the same as the experimental bathymetry and the chosen slope is 1:1. The experimental and the numerical results are compared at gauges 1, 3, 8 and 11. The spatial locations for

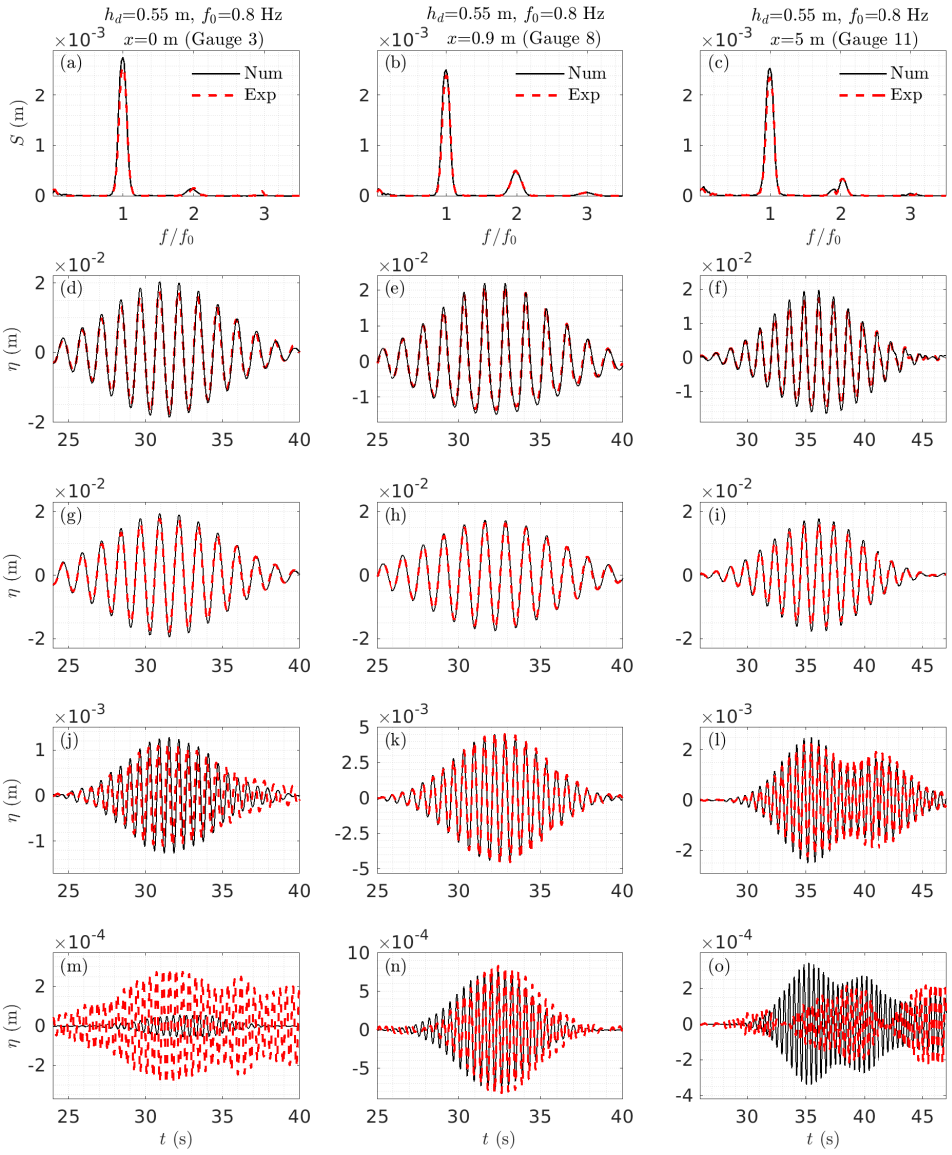


Figure 3.4: Comparison between numerical wave groups and experimental wave groups at different gauges. Comparison between the spectrum of numerical and experimental results for (a, b, c), for (d, e, f) the comparison between experimental wave group and numerical wave group generated using two relaxation zones and one itertaion, for (g, h, i) the first-order harmonics, for (j, k, l) the second-order harmonics and for (m, n, o) the third-order harmonics. η is the surface elevation and f_0 is the peak frequency. t is time, and x indicates the distance to the top of the slope.

these 4 gauges are presented in Table 3.4. After trying different methods to generate the waves in the numerical tank, we find the agreement between the numerical and the experimental results are the best if we use two relaxation zones with one iteration for wave generation. The iterative method is described in §3.3.1. Thus the comparison at gauge 1 is a test of how accurate we are in initialising our simulations.

In Figure 3.4(d, e, f) show the comparison between the experimental and the numerical results at gauge 3, 8 and 11, respectively. We find that the agreement between experiment and simulation is acceptable at all of these three gauges. However, there are small discrepancies, which are further analysed below.

In Figure 3.4(a, b, c), the amplitude spectrum of numerical and experimental results at gauge 3, 8 and 11 respectively are presented. Figure 3.4(a, b, c) show the agreement of the spectrum between experimental and numerical results is good at all three gauges including importantly the higher harmonics after the step. In order to evaluate the different-order harmonics, frequency filtering is used. In Figure 3.4(g, h, i) and (j, k, l), the first-order harmonics and the second-order harmonics are presented at gauges 3, 8 and 11, respectively. At first and second order, agreement between numerical and experimental results is excellent, and there is no large difference at any gauge. However, for the third order harmonics, shown in Figure 3.4(m, n, o), there are significant discrepancies. The agreement at gauge 8 is good, whereas, at gauge 3 and 11, there is a difference between the experimental and numerical results. One possible reason for this mismatch is the beating effect predicted by Li's theory (Li et al., 2021b), which are sensitive to small errors in position although this explanation is not fully satisfactory. The amplitude of third order harmonics are relatively small. Thus, the difference is not apparent in Figure 3.4 (d, e, f).

The results presented here are typical for the other cases considered in Li et al. (2021a). We have not attempted to simulate the 'step' case as we cannot have a perfect step in the OW3D code.

3.6 Kinematics of wave over variable bathymetry

Having established the accuracy of the code, we now consider the kinematics of the fluid after the slope. Whilst there is a large literature on waves over slopes, little attention has been paid to the kinematics (they are briefly considered in Lawrence et al. (2021b)) despite the kinematics being critical to loads on structures. Unlike some other numerical schemes (particularly HOS) where kinematics are usually found by post-processing and are not explicitly solved for, OW3D does solve for the water particle movements within the domain.

In the present analysis, we continue to investigate the same case as the validation test and we select a specific region in the numerical domain to study the wave kinematics. We focus on the kinematics from 20 m to 25 m on the horizontal axis and traverses the full depth (z-direction) of the numerical domain.

Figure 3.5 shows the total velocity at a specific time step (t=31.6 s) for the same case as the validation case. We find the velocity increases locally at the top of the slope, and the maximum velocity occurs some distance after the slope. This appears to be consistent with the theory developed by Li et al. (2021c), in which large waves are predicted when the released second-order waves and linear waves come into phase. At the top of the slope itself, there appears to be a localised large velocity near the sea-bed. This is an unsurprising feature of the analysis–one would not expect the classic distribution of wave velocities over the water column at a sharp discontinuity. In fact what is interesting is how localised this is. This helps explain why simplified models which ignore local effects such as Massel (1983) show good agreement with numerics and experiments.

We now briefly consider the impact of wave kinematics on loads on offshore wind turbines. Following the recent work of Klahn et al. (2021), we use the kinematics to calculate the loads on an offshore structure. Monopiles are common types of offshore structures (e.g., offshore wind turbines), and we can evaluate the wave loading on

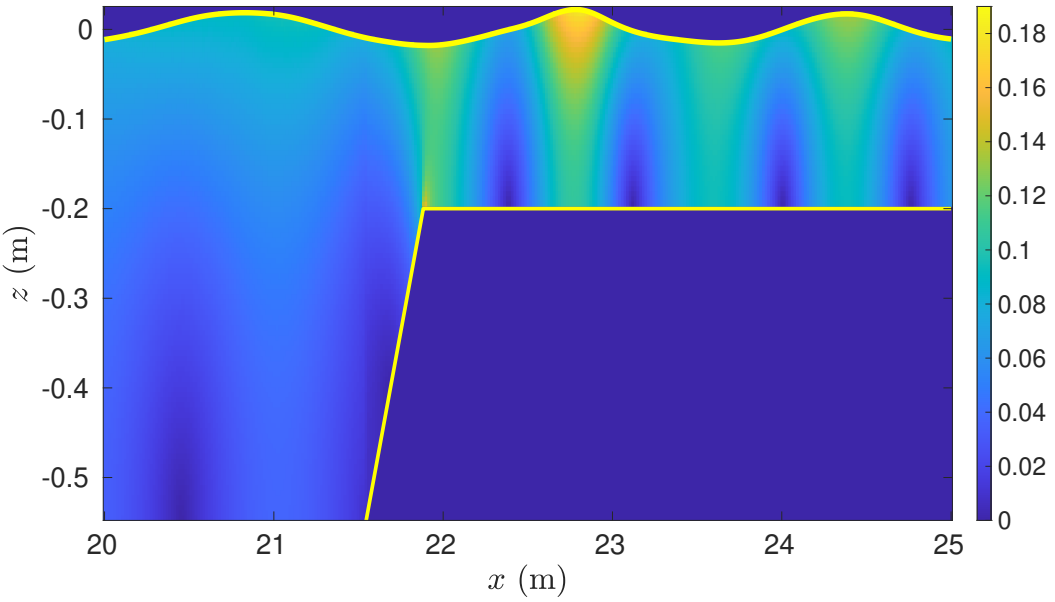


Figure 3.5: Total velocity (m/s) at different horizontal and vertical location at t=31.6 s. x and z represent horizontal and vertical locations. The magnitude of the total velocity corresponds to different colors, shown in colorbar.

slender structures based on the kinematics in the absence of the structure (Dean and Dalrymple, 1991). The inertial force is one component of the wave loading and caused by the acceleration of the flow. The inertial force is dominant for cylinder whose diameter is 0.2 times larger than the representative wave-length ($D/\lambda > 0.2$). In this case, a diameter of the cylinder (D) of 0.5 m is selected and the inertial force on the cylinder can be calculated by Morison's equation (Morison et al., 1950).

$$F(x,t) = \rho \frac{\pi D^2}{4} C_M \frac{\partial u}{\partial t}, \tag{3.6}$$

where $F(x,t)$ is force per unit length on a fixed vertical cylinder located at a specific spatial location (x), ρ is the water density, C_M is the inertial coefficient (C_M = 2) and $\partial u/\partial t$ is the time derivative of the horizontal velocity at corresponding time and space. We note that the Morison calculation is a simplified one–models such as Rainey (1989) contain more physics including better modelling the higher order harmonics

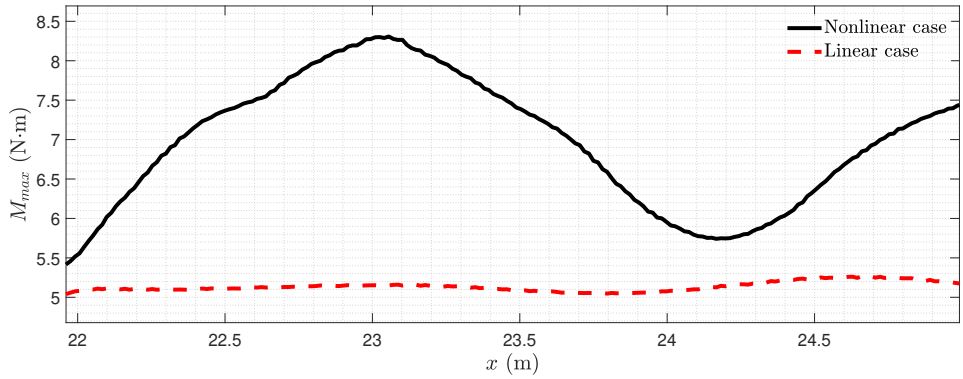


Figure 3.6: Maximum value of the envelope of the moment (M_{max}) at different spatial location (x) for a cylinder whose diameter is 0.5 m. The top of the slope 21.88 m. In the nonlinear case, nonlinear terms of the free-surface boundary conditions are included in the simulation, and in the linear case, numerical waves follow linear wave theory.

of the loads (Chau and Eatock Taylor, 1992; Huseby and Grue, 2000; Feng et al., 2020). We choose to examine the moment on the cylinder around the sea-bed as this is typically the critical load for structural and geotechnical design of such structures.

After calculating the moment on the cylinder at each time step and each spatial location, we can find the maximum value of the envelope of the moment at each spatial location (from x=21.88 m, the top of the slope, to x=25 m). We run two simulations: one uses the linear version of the code, whereas the other solves the fully non-linear equations. Figure 3.6 shows the maximum value of the envelope at each spatial location. In Figure 3.6, the linear case and nonlinear case are compared to investigate the influence of the slope on the higher-order harmonics waves of the wave group. We find the maximum value of nonlinear case is larger than that of linear case on the shallower water side. It means the slope not only amplifies the wave crest, but also increases the wave kinematics and the moment on the cylinder. We also see a 'beating' pattern forming (see for instance Monsalve Gutiérrez (2017)) which is consistent with the model that amplifications in response are caused by the release of bound waves. Whilst not investigated here, we note that offshore wind turbines are typically designed so that the resonant frequency is double or treble typical storm

waves (Kallehave et al., 2015). Thus loading from released higher harmonics will be particularly important to understand for design.

3.7 Conclusions

In this paper we have shown OceanWave3D can be used to model waves passing over varying bathymetry including very sharp changes in bathymetry which have attracted considerable interest as a mechanism for generating abnormal waves. We show the code is numerically accurate for modelling such cases. We also show that there is generally very good agreement between numerics and experiments except for the very small third-order components. The accuracy of OceanWave3D appears to be primarily dominated by the timestep at least for the values considered herein.

Although steps have been shown to produce abnormal waves at the top of the slope, these have not so far been linked to loads on structures. Here, we use the kinematics from our numerical simulations to do this. We show that loads on offshore structures are significantly enhanced by the non-linear physics as waves pass over steep slopes, which is of potential concern to offshore engineers.

Statement of Authorship

Title of Paper:	On Rogue Waves Generated by Abrupt Depth Transitions
Publication Status	Published
Publication Details	*Li Z, Tang T, Draycott S, Li Y, van den Bremer T, Adcock T (2022) On Rogue Waves Generated by Abrupt Depth Transitions. In: 41st International Conference on Ocean, Offshore & Arctic Engineering, OMAE2022*
Student Confirmation	
Student name:	Zhenhao Li
Contribution to the paper	*performed simulations of Oceanwave3D, analyzed data, wrote manuscript*
Signature:	Date: 6/3/2023
Supervisor Confirmation	
Supervisor name and title:	Professor Thomas Adcock
Signature:	Date: 6/3/2023

Chapter 4

Wave loads on ocean infrastructure increase as a result of waves passing over abrupt depth transitions

4.1 abstract

Abrupt changes in water depth are known to lead to abnormal free surface wave statistics. The present study considers whether this translates into abnormal loads on offshore infrastructure. A fully non-linear numerical model is used which is carefully validated against experiments. The wave kinematics from the numerical model are used as input to a simple wave loading model. We find enhanced overturning moments, an increase of approximately 20%, occur over a distance of a few wavelengths after an abrupt depth transition. We observe similar results for 1:1 and 1:3 slopes. This increase does not occur in linear simulations.

4.2 Introduction

Ocean waves are central to the study of ocean engineering and are a key design driver for many marine energy devices. Standard models of wave statistics assume that the underlying freely propagating components are uncorrelated. However, situations may arise where correlations are present between components, and this leads to a greater number of large waves than would otherwise be expected. Such waves can be considered rogue or freak waves (see reviews by Dysthe et al. (2008); Adcock and Taylor (2014)).

One mechanism which can cause an increased number of large waves is where waves propagate over a rapid change in water depth. This mechanism was identified a decade ago (Trulsen et al., 2012) and has since motivated many researchers (Gramstad et al., 2013; Ducrozet and Gouin, 2017; Bolles et al., 2019; Zhang et al., 2019; Zheng et al., 2020; Monsalve et al., 2022). One mechanism that has been proposed attributes the enhanced number of large waves to the interaction between second-order bound and the free waves additionally released due to a depth transition (Li et al., 2021b,c). For a train of Stokes waves experiencing abrupt depth transitions, a second-order theory was derived by Massel (1983), in agreement with the experimental observations by Monsalve Gutiérrez (2017). Li et al. (2021c) and Li et al. (2021b) have extended the theory to allow for a narrowband wavepacket and a statistical analytical model for a train of irregular random waves, respectively. These have been found to be in good agreement with both numerical and laboratory observations. An alternative explanation, which may also be important, or indeed coupled, is that sea-states are pushed out of equilibrium leading to an increase in rogue waves as the sea-state adjusts to the new equilibrium (e.g., Zeng and Trulsen (2012); Viotti and Dias (2014); Mendes et al. (2022)). Such effects can also contribute to the number of extreme waves generated.

The focus of most of the past work has been on free surface wave statistics. How-

ever, for practical engineering purposes such as loading on offshore wind turbines, the wave kinematics may be of greater interest, as they are more closely related to the loads. Recent research has started to investigate the wave kinematics. A new method for the calculation of water-particle kinematics based on the fully nonlinear Variational Boussinesq model was developed and applied to the problem of waves propagating over a slope by (Lawrence et al., 2021a; Trulsen et al., 2020). The statistics of wave kinematics in long-crested irregular waves propagating over a shoal is studied by Lawrence et al. (2021b) using a Monte Carlo approach. The evolution of kurtosis and skewness of the horizontal velocity is discussed, and the statistical properties are compared to laboratory experiments. Trulsen et al. (2020) conduct the experiments of long-crested irregular water surface waves propagating over a shoal. The location of local maximum and local minimum of skewness and kurtosis are investigated in terms of the surface elevation and the horizontal fluid velocity. In addition, Bateman et al. (2003) investigate the calculation of the water particle kinematics generated by the propagation of surface gravity waves.

Our work seeks to examine the wave kinematics and loads induced on an idealised structure in the vicinity of an abrupt depth transition. We use fully non-linear potential-flow simulations which explicitly solve for the wave kinematics.

4.3 Numerical and experimental methodology

4.3.1 Experimental setup

In this paper, the experimental data is taken from Li et al. (2021a,b). In the experiment, only surface elevation is measured. The experimental set-up is presented in Figure 4.1. A total of 16 gauges were used to measure the waves and the locations of 16 gauges are shown in Table 4.1. Our study primarily focuses on the results at gauges 1, 3, 8 and 11 and the measurements at these 4 gauges are selected for comparison

Gauge no.	1	2	3	4	5	6	7	8
Position x (m)	-1.88	-0.10	0.00	0.10	0.30	0.50	0.70	0.90

Gauge no.	9	10	11	12	13	14	15	16
Position x (m)	1.10	1.50	5.00	7.50	10.0	14.0	15.0	18.0

Table 4.1: The locations of 16 gauges in the experiment. Position x indicates the distance to the top of the slope, and positive value indicates gauges after the top of the slope (from Li et al. (2021a)).

with the numerical simulations. The width of the flume is 0.6 m and the length is 35 m. The top of the slope is 7.5 m away from the wave-maker. The water depth of the deeper water side, h_d, is 0.55 m and the water depth of the shallower water side, h_s, is 0.2 m. Thus the height of the slope is fixed as 0.35 m. The slopes are indicated by the dashed lines in Figure 4.1, showing a slope of both 1:1 and 1:3.

4.3.2 Numerical set up

OceanWave3D (OW3D) is used to model the waves (see Engsig-Karup et al. (2009)) and the governing equations of OW3D are shown in appendix A.

Potential-flow equations for surface gravity waves are solved by OW3D in a three-dimensional Eulerian frame, which gives the kinematics information not only at the free-surface boundary but also at all the vertical nodes hence allowing full kinematic reconstruction. Thus, the wave kinematics are extracted directly during the time-marching process without any further assumptions. A classical fourth-order Runge–Kutta time marching-scheme is used. A σ-coordinate transformation is applied to

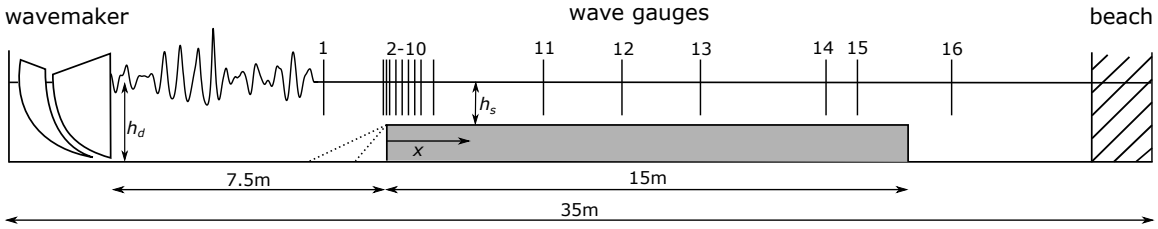


Figure 4.1: Diagram of experimental set-up including gauges, step, beach and wave-maker positions (from Li et al. (2021b)).

map the vertical solutions to a time-invariant grid, which can also be used to solve the fully nonlinear potential-flow equations with variable bathymetry. Wave breaking is implemented using a local smoothing function. This local smoothing function monitors the particle downward acceleration of the free surface (monitoring the Lagrangian particle acceleration in the governing equations of OW3D) and it removes a small amount of energy locally until the acceleration is below the threshold. In our simulation, the local smoothing function is triggered when the detected acceleration is greater than $0.4g$ (where g is the gravitational acceleration), which follows previous work (Tang et al., 2021). Interestingly, in this study, we have experienced unusual breaking events especially around the abrupt depth transitions. These strong breaking waves caused difficulties to get convergence with this simplified breaking model, which helps further stabilise the numerical scheme. The simplified breaking model can only be applied once at each time step. Thus, we found a small number of events occurred where, it is presumed, the wave was breaking caused the code to stop. This suggests that breaking at the top of the slope may have significant differences from waves on a flat bathymetry, which is consistent with the recent work of Draycott et al. (2022). When the code stops, a finer resolution in temporal domain is applied to allow the breaking model to trigger over more timesteps allowing the code to compute through the point at which it could not converge with the normal time step. After passing this point, we change to the original resolution until meeting the next crash point. The model also has a 'linear' version which we use in this paper. This version solves the classic linear form of the water wave equations. In the linear model of OW3D, the surface elevation profile is set to zero in the σ-coordinate transformation and the nonlinear terms in the free-surface boundary conditions were also neglected, which leads to generated waves follow the linear wave theory (see Bingham and Zhang (2007) for detailed implementation of this model).

The numerical domain is almost identical to that used in the experimental case,

and the relative location of gauges is the same as in the experiment. In our numerical domain we use gauge 3 as our datum (x =0 m in the numerical domain) so locations upstream of this are negative. In our simulations, the peak frequency of the input waves is 0.8 Hz. The wavelength is 2.23 m and 1.6 m on deep and shallow side, respectively. The water depth on the deep side and shallow side is 0.55 m and 0.2 m, respectively, which is the same as experimental setup. we consider two different slopes: a slope of 1:1 and one of slope 1:3. The input waves and numerical domain are the same for both cases. The length of the numerical domain, L_x, is 54 m (from x =-21.88 m to x =32.12 m a length of 24 wavelengths) and the number of nodes on the x-axis, N_x, is 3500. The number of nodes on the z-axis, N_z, is 20. The timestep, Δt, is 0.03125 s (40 time steps per wave period) and a total time duration of 3.5 hours of wave propagation is simulated for both cases. Waves are generated using a double relaxation zone to help absorb reflected waves, which is located from -21.88 m to -1.88 m (9 wavelengths). At the end of the domain, waves are absorbed using a pressure boundary condition. Thus, a damping zone is applied at the end of the domain and the length is 10 m (from x =22.12 m to x =32.12 m and corresponding to 4.5 wavelengths). The top of the slope is located at x = 0 m in the numerical domain for both cases, which is 1.88 m away from the end of the relaxation zone ($x = -1.88$ m). The same numerical setup is adapted for both linear and non-linear model of OW3D simulations. The steepness of the slope is changed by changing the length of the slope. The discretisation used is based on the study of Barratt et al. (2020) and a grid convergence study on the same geometry used here is presented in Li et al. (2022b).

4.3.3 Input waves

In this paper, we primarily consider random wave simulations. In the experiments, the waves are drawn from a JONSWAP spectrum with peak enhancement factor,

γ = 3.3, and the JONSWAP sepctrum is developed by Hasselmann et al. (1973):

$$S(\omega) = \frac{\alpha g^2}{\omega^5} \mathrm{e}^{-5/4(\omega_p/\omega)^4} \gamma^{\exp\left(-1/2(\omega-\omega_p/s\omega_p)^2\right)}, \tag{4.1}$$

in which ω_p is the peak frequency ($\omega_p = 2\pi/T_p$) and the parameter s =0.07 for $\omega < \omega_p$ and s =0.09 for $\omega > \omega_p$. The input measured significant wave height at the first gauge of the experiments was H_s =0.045 m giving a significant steepness of $\frac{1}{2}H_s k_p$ = 0.064 (the peak wave number, k_p, is 2.81m^{-1} on the deep side). The peak frequency of the input waves is 0.8 Hz giving a non-dimensional water depth on the deep side of $k_p h_d$ = 1.55 and, assuming linear shoaling, a non-dimensional depth on the shallow side of $k_p h_s$ = 0.79. In our simulations, the experimental data at gauge 1 are used as input for the OW3D simulations. We ignore the first 300 seconds of the experiment to allow the waves to reach a steady state.

4.4 Validation against experiments

Extensive verification and validation, in addition to a convergence study, of the model used in the present paper was undertaken in Li et al. (2022b) and is not repeated here. This previous work focused on deterministic wave groups rather than random waves as are studied here. As such, we here focus on the aspects of the modelling that apply to random waves but not to deterministic groups. These aspects are principally the wave generation and wave breaking (as the groups in the previous work were designed not to break). We note that the wave generation in the numerical model is different from that in the experimental model. In addition, this potential-flow solver can never fully capture the non-potential–flow physics induced by wave breaking (e.g., Eeltink et al. (2022)) and vortex shedding due to the sharp edge at the top of the slope. The experiments and numerics will also differ in that some dissipation from the side walls will occur in the experiments and also differ in wave absorption with more complete

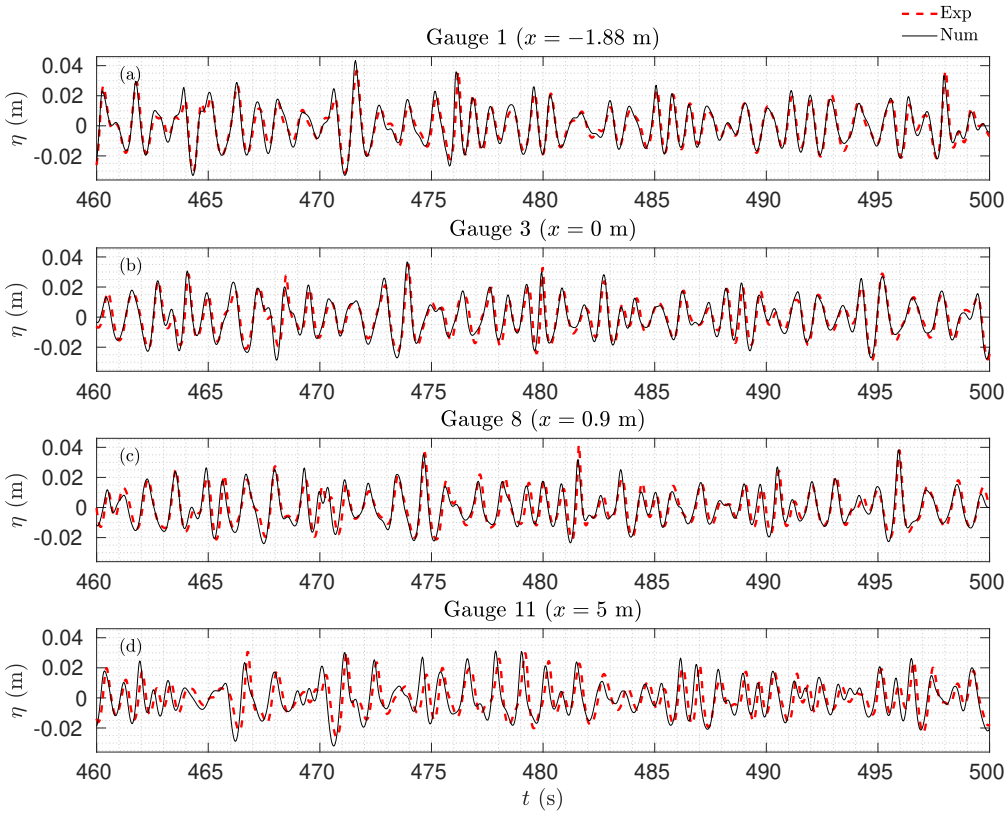


Figure 4.2: Representative time histories of surface elevation at different gauges comparing experimental and numerical result (1:1 slope case), where x indicates the distance from the top of the slope, η the surface elevation and t time.

absorption being expected in the numerical scheme. Another expected source of inaccuracy is that we use experimental data at gauge 1 as input to the numerical model. However, this data includes waves reflected off the depth transition which are travelling in the opposite direction. In our validation we present results for the 1:1 slope as similar results are observed for the 1:3 case and intuitively the latter case is expected to be marginally easier to simulate as non-linear physics is likely to be less severe.

Despite the aforementioned limitations due to the potential-flow solver used, we generally find good agreement between experiments and numerics. Figure 4.2 shows a representative time series of the free surface η for the 1:1 slope case at several gauges. Given the differences between experiment and numerics, the agreement is generally good. Waves are well aligned in time and the magnitudes are adequately captured. The differences between the numerically generated waves and experimental results at Gauge 1 can be attributed to various causes. We assume all the wave component measured at Gauge 1 during experiments are propagating downstream, whereas they are actually composed of both incident waves and reflected waves from the step and from the beach during the experiments. The numerical results measured at the end of relaxation zone also include reflections, especially from the slope, which also contribute to the deviation. We have applied a double relaxation zone to absorb these reflections but there is also a compromise between being able to make the exact waves and reducing the influence of reflected waves. There also seems to be a systematic horizontal shift especially at gauge 11. One of the reasons for this can be the minor error between experiments and simulations in terms of the exact location of gauges or the slope. Bed and sidewall frictions could also contribute to horizontal shifts at far away gauges.

Next we look at the significant wave height H_s at our four gauges. The significant wave height is defined by the mean of the largest 1/3 of the waves and the individual

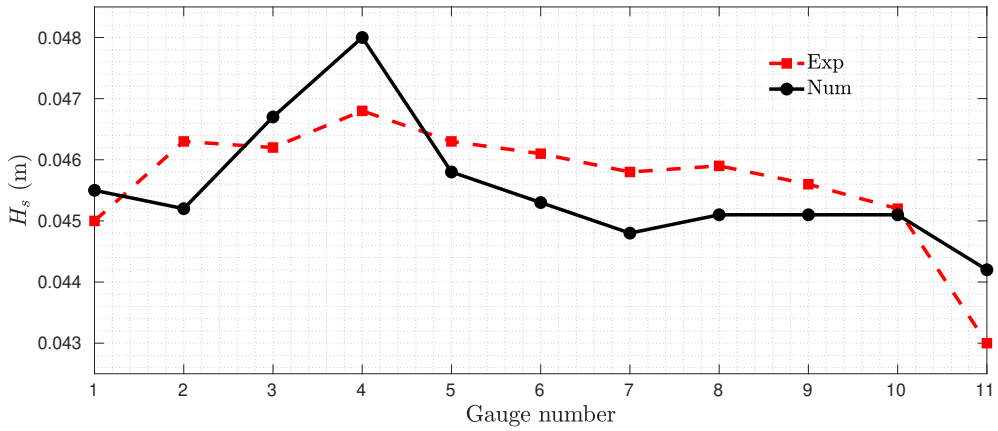


Figure 4.3: The significant wave height H_s at different gauges for numerical and experimental results (1:1 slope case)

wave is determined by zero up crossing. The significant wave height of numerical and experimental results are shown in Figure 4.3. In terms of the experimental and numerical results at gauge 1, 3, 8 and 11, they are shown in Table 4.2. Our simulations are based on the experimental results at gauge 1. The 1% difference in H_s at gauge 1 is a result of combined reasons mentioned above and the discrepancy at all locations is small with both experiment and numerics showing similar trends.

Gauge no.	1	3	8	11
Numerical H_s (m)	0.0455	0.0467	0.0451	0.0442
Experimental H_s (m)	0.0450	0.0462	0.0459	0.0430
Relative differences (%)	1.1	1.1	1.7	1.9

Table 4.2: Significant wave height (H_s) of numerical (1:1 slope case) and experimental results at gauge 1, 3, 8 and 11

We now turn to height statistics. Figure 4.4 presents the probability that a given wave height is exceeded at a particular location. We include both fully non-linear simulations as well as otherwise identical simulations using the linear model. The agreement between non-linear simulation and experiment is generally good, showing similar departures from the Rayleigh distribution and linear simulation after the step. The Rayleigh distribution without modification is based on a narrow-band assumption and it is the most commonly adopted distribution for the crest to trough wave heights

as well as the starting point for many other models. The exceedance probability of wave height follows the Rayleigh distribution for narrowbanded linear waves. The Rayleigh distribution is given by:

$$\Pr = -\exp\left(-\frac{H^2}{8m_0}\right), \tag{4.2}$$

where m_0 is the zeroth-order moment of the spectrum and this equation describe the probability of a wave height is bigger than a given wave height H.

Although within the confidence intervals, the numerical simulation does seem to slightly under-predict the number of large waves at gauge 8 (x = 0.90 m) and more clearly (although still within confidence intervals), does so at gauge 11 (x = 5.00 m) some way after the change in depth. This contrasts with a smaller over-prediction by the non-linear model at gauges 1 and 3. Given the multiple minor differences in setup between experiment and simulation, it is hard to identify the reason for these small differences. However, agreement is sufficient to have confidence in our simulation. There is also an unexpected discrepancy between the linear simulations and the Rayleigh distribution at gauge 11.

We also consider the average shape of an extreme event. Although here we are primarily using this for validation, this is, to our knowledge, the first time this has been examined for the wave over a steep slope problem. In our analysis, we are focused on the average shape of an extreme event at gauges 1, 3, 8 and 11. Based on our simulation results, there are approximately 12,000 waves at each gauge in both the 1:1 and 1:3 slope cases. We find the largest 40 waves measured at each gauge and find their average shape. The number of waves chosen is a trade off between capturing the extremes and statistical variability. Under a theoretical linear model, the expected shape of an extreme event is given by the scaled autocorrelation function

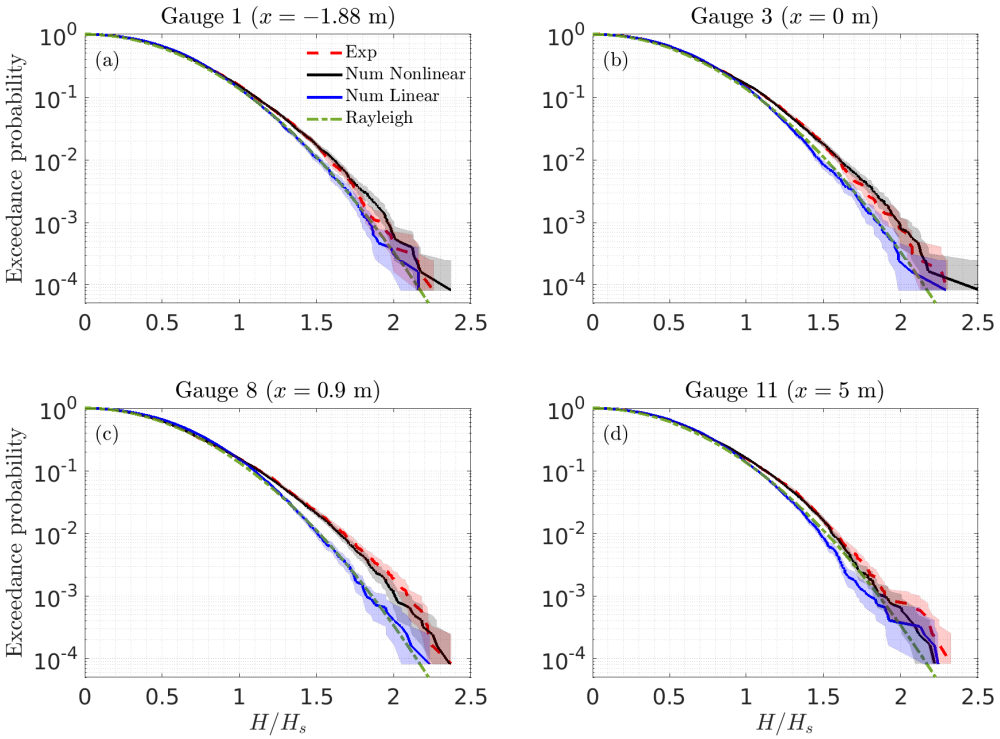


Figure 4.4: Comparison of experimental and simulated wave height statistics with 90% confidence intervals at gauge 1, 3, 8 and 11 for the 1:1 slope case. Wave heights (H) are normalised by the significant wave height (H_s)

– the 'NewWave' (Lindgren et al., 1970; Boccotti, 1983; Tromans et al., 1991).

$$\eta(t) = \frac{1}{m_0} \int_0^\infty E(f) \cos(2\pi f t) \mathrm{d}f, \tag{4.3}$$

in which $E(f)$ is the spectrum, and m_0 is the zeroth-order moment of the spectrum. f is the peak frequency, and t is time. $\eta(t)$ indicates the NewWave profile. The linear model predicts a symmetric wave packet around an extreme event. Deviation from the linear model is expected at all gauges as bound harmonics will significantly modify the shape. However, we include the linear-model prediction for reference.

We analyse the resulting shape in Figure 4.5. At the input gauge 1, there is a minor asymmetry in the numerical simulations. At gauge 3 (at the top of the slope) both numerics and simulation suggest some minor asymmetry with the trough preceding a large wave being slightly deeper than that following it. Gauge 8, roughly half of the wavelength after the top of the slope, shows some clear discrepancies from the standard 'NewWave shape'. The trough preceding the largest wave is relatively sharp whereas, at this location, the trough after is far flatter. This is consistent with the shape observed for deterministic wave groups and has been explained by the release of bound waves at the step (Li et al., 2021b). Both experiments and numerics show similar results suggesting strongly that the simulations are capturing the physics of bound wave release. The results at the final gauge (gauge 11), after the point we are primarily interested in, show the waves returning to a more standard symmetrical shape although some deviation from this can still be seen in both experiments and numerics. There are also some significant differences between the shapes predicted computationally and observed experimentally at gauge 11 (as results for wave height statistics also suggested). It is unclear why there is this difference. However, gauge 11 is beyond the main area we are interested in, so whilst we note the discrepancy we do not think this should invalidate the main conclusions of this paper.

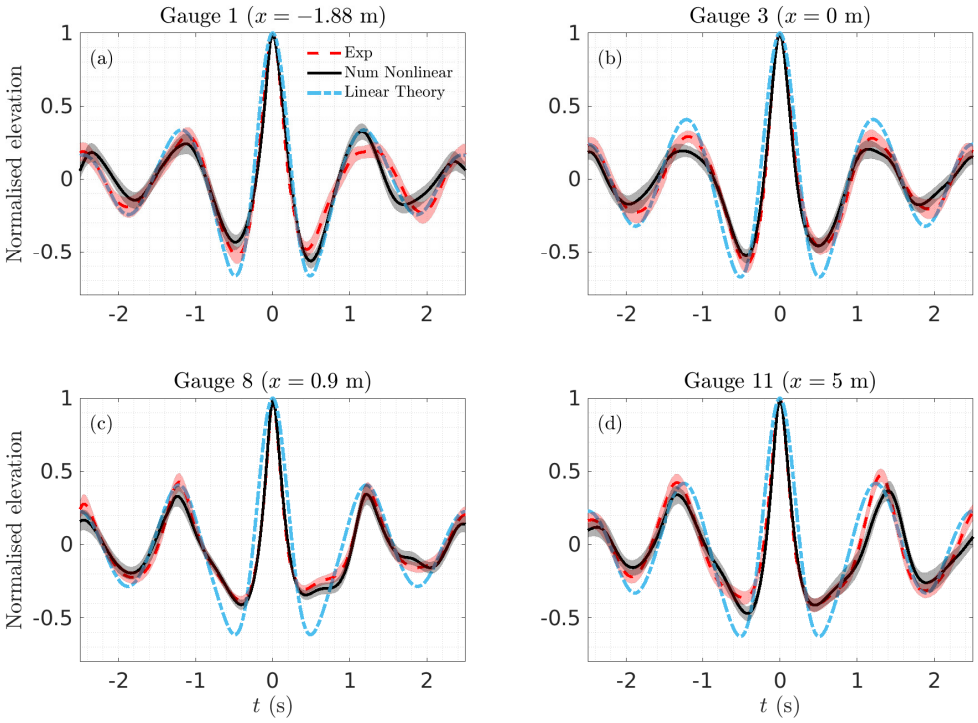


Figure 4.5: Average of the 40 large crests normalised by the value at the largest crest for the 1:1 slope case with 90% confidence intervals, where t is the time relative to the largest crest and x indicates the distance from the top of the slope

4.5 Results

We consider the engineering aspects of the enhanced rogue wave activity at the top of slopes. There are many different wave/structure interactions one could consider all with their different characteristics. In the present paper we consider a simplest model of waves interacting with a column as this is a useful general example. For simplicity we follow the general taken recently by Klahn et al. (2021) of using a model based only on the fluid kinematics so as to avoid having to solve any complex wave/structure interaction problem. The choice of this model is not critical to the conclusions of this paper – the aim is to do a calculation which relies on the kinematics rather than the free surface considered in most studies.

We model the structure using the drag term of the Morison's equation (Morison et al., 1950). In this case, a monopile of a diameter (D) of 0.5 m (D/λ = 0.225) is selected, and the load per unit length on the monopile is a function of the undisturbed horizontal velocity, which is given by:

$$F(x,t) = \frac{1}{2}\rho D C_D u|u|, \tag{4.4}$$

where $F(x,t)$ is the force per unit length on a fixed vertical cylinder located at a specific spatial location x, ρ is the water density, C_D is the drag coefficient (C_D = 1.2) and u is the horizontal velocity at corresponding time and location.

We choose to analyse the moment around the sea-bed as this is probably the most important feature for the design of a typical offshore structure. From the OW3D simulations, we calculate the horizontal velocity. We can calculate the total moment around the sea-bed by integration before calculating the peak moment in each loading cycle. We only consider this after the top of a slope as the different water depths before this point would confuse the analysis as the change in the sea-bed depth would dominate the change in moments. In Figure 4.6, moment exceedance is presented for

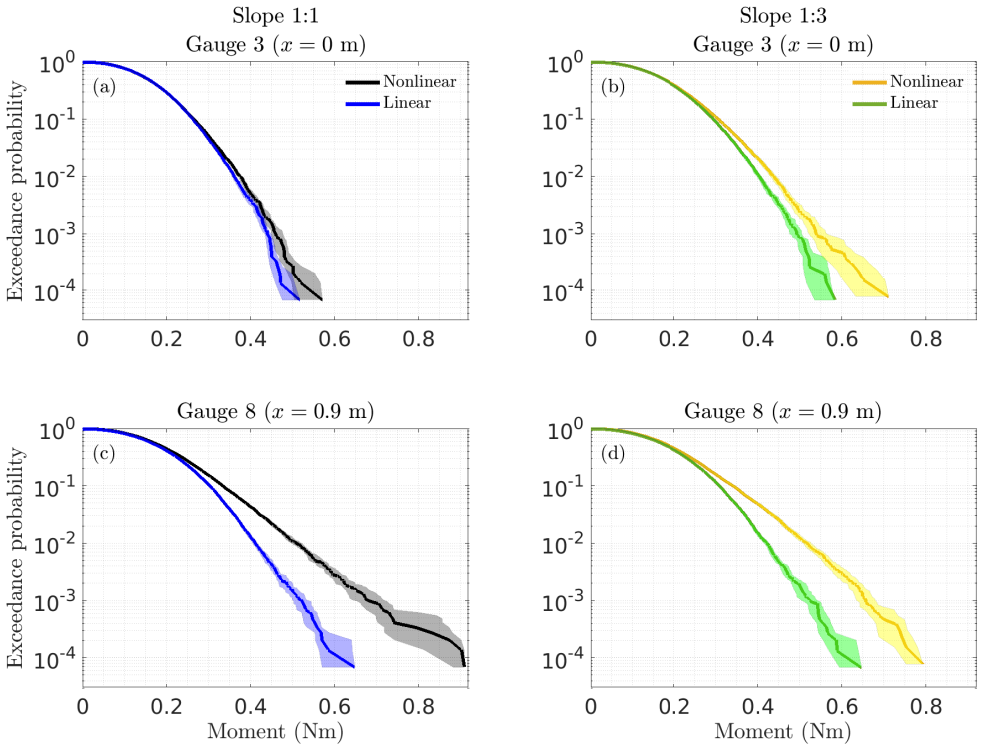


Figure 4.6: Comparison of moment statistics for slope 1:1 and slope 1:3 at gauge 3 and 8. Two gauges are shown with 90% confidence intervals. Moment is the total moment around the sea-bed after the slope.

gauges 3 (top of slope) and 8 (slightly after top of slope) and both 1:1 and 1:3 slopes showing both linear and non-linear simulation results. The linear simulations predict very similar moments in all cases and these are always lower than that predicted by the non-linear model. However, the departure from the linear is very much larger for gauge 8 than just at the top of the slope at gauge 3. This difference is greater for the steeper slope (1:1 case). Interestingly, at gauge 3 there is a bigger difference between linear and non-linear for the milder slope (1:3 case), likely due to the different phase shifts of second-order bound and free waves between the two cases. At the top of a slope, a steeper slope may lead to the second-order waves more out of phase and therefore smaller amplitude of second-order waves. As a consequence, it would lead to smaller differences between the nonlinear and linear simulations for a steeper slope case, as noted. This finding is consistent with the observations in both Li et al. (2021b) and Zheng et al. (2020) due to the following. The former found both a larger skewness and kurtosis at gauge 3 for the case of 1:3 slope (i.e. their Fig.2 and Fig.3) compared to the case of 1:1 slope. Zheng et al. (2020) (i.e., their table VI) suggests a slope gradient plays an important role in the location of the peak kurtosis and skewness relative to the top of a slope, which is the furthest and nearest for the steepest slope (a step) and the mildest slope, respectively.

To analyse extremes we consider the overturning moment which corresponds to the 1-in-1000 wave event. Thus, in Figure 4.7, the moment is the moment corresponding to a probability of 10^{-3} in the moment exceedance figure as a function of spatial location.

We see very similar behaviour for both slopes except in the non-linear simulations very near the top of the slope where higher loads are predicted for the flatter (1:3) case. This may be the result of a slightly higher significant wave height for the flatter case due to less breaking in OW3D. However, the moment behaviour is consistent with the previous work on this setup where very similar physics was found for the

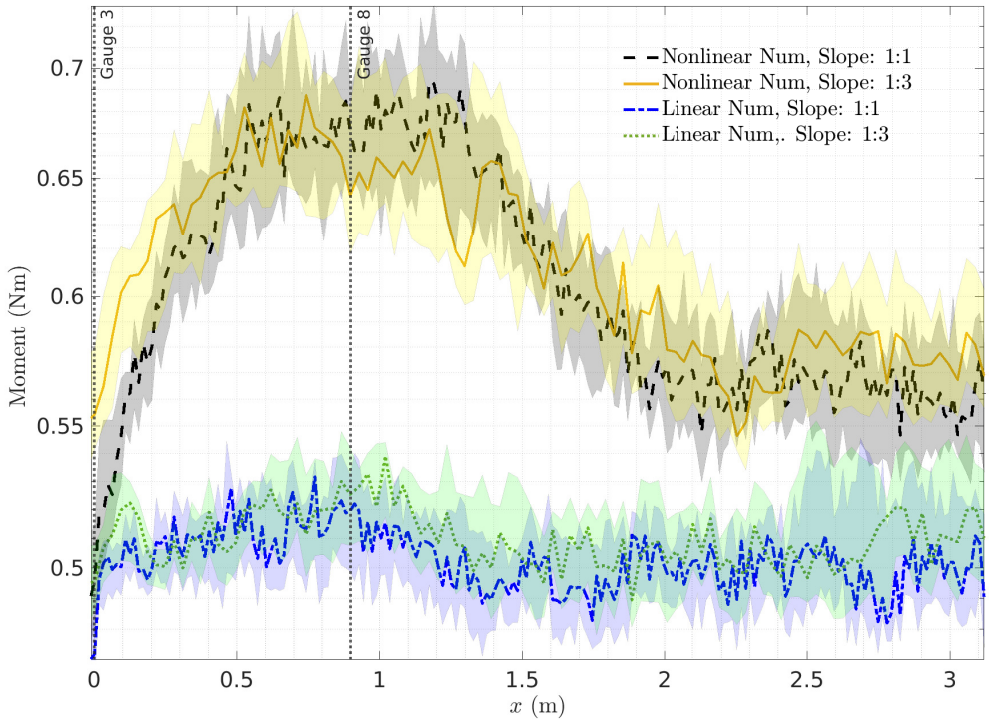


Figure 4.7: Overturning moment about the sea-bed predicted by the numerical model. 90% confidence intervals are shown. The moment is the moment corresponding to the probability of 0.1% (one-in-1000 wave) in the moment exceedance figure for different spatial locations. The locations of gauge 3 (At the top of the slope) and gauge 8 (0.9 m after the top of the slope) are indicated by dotted black lines.

two slopes. There appears to be enhanced moment around the top of the step, which increases approximately 20%, consistent with the increased number of large waves observed in both simulation and experiment. The 'peak' in this lasts for several wavelengths beyond the top of the slope before decreasing and plateauing. The non-linear simulations consistently predict larger moments than the linear ones. However, the linear simulations do not produce a significant peak and are essentially uniform across the region considered. Thus we can have confidence that the peak in the moments observed is the result of non-linear physics.

4.6 Conclusions

This paper has related the theoretical problem of excess rogue waves occurring at the top of slopes to a practical problem in ocean engineering. In doing so, this enables us to draw the following conclusions regarding the wave kinematics of the problem.

We have run a fully non-linear potential-flow model which directly solves for the wave kinematics. This model has been found to be in good agreement with experimental results for surface elevation including for the expected shape of an extreme wave events which to our knowledge has not previously been studied. We then use these kinematics to drive a simple wave loading model. We find enhanced loads (around 20% larger than linear simulation) for several wavelengths after the abrupt depth transition. This study suggests that extra care is needed when designing ocean infrastructure at the top of slopes and that the abnormal free surface wave statistics previously observed at the top of slopes also lead to unusual moment or unusual kinematics occurred at the top of the slope.

Statement of Authorship

Title of Paper:	Wave loads on ocean infrastructure increase as a result of waves passing over abrupt depth transitions
Publication Status	Published
Publication Details	*Li Z, Tang T, Li Y, Draycott S, van den Bremer TS, Adcock TA (2022) Wave loads on ocean infrastructure increase as a result of waves passing over abrupt depth transitions. Journal of Ocean Engineering and Marine Energy pp 1–9*
Student Confirmation	
Student name:	Zhenhao Li
Contribution to the paper	*performed simulations of Oceanwave3D, analyzed data, wrote manuscript*
Signature:	Date: 6/3/2023
Supervisor Confirmation	
Supervisor name and title:	Professor Thomas Adcock
Signature:	Date: 6/3/2023

Chapter 5

Directionally spread wave groups propagating over an abrupt depth transition

5.1 Introduction

Scientists and engineers are interested in the large ocean waves as these play an important role when it comes to the design for marine infrastructure. In some circumstances, the probability of the large ocean waves is underestimated when using the linear wave dynamics to predict the probability of extremes. When the underlying freely propagating components are correlated, there are a greater number of large waves and these abnormally large waves may be regarded as the rogue waves (Dysthe et al., 2008; Adcock and Taylor, 2014). Various physical mechanisms have been investigated and considered to explain rogue waves (Kharif and Pelinovsky, 2003; Onorato et al., 2013; Adcock and Taylor, 2014). Waves propagation over an abrupt depth transition is one of the physical mechanisms to explain rogue waves, and it has been extensively investigated over past decade (Sergeeva et al., 2011; Trulsen et al., 2012;

Gramstad et al., 2013; Bolles et al., 2019; Zheng et al., 2020).

Two main theories have been developed to explain the influence of the abrupt depth transitions on the formation of the rogue waves. According to Li et al. (2021b,c), second-order free waves are released after the depth transition, and the interaction between the second-order bound wave and the second-order free wave leads to the rogue waves. The release of free waves has been observed in both experiments and simulations (Li et al., 2021b). An alternative explanation is that the sea-states are pushed out of equilibrium and are forced to adjust to a new equilibrium state, which leads to the rogue waves (Zeng and Trulsen, 2012; Viotti and Dias, 2014; Mendes et al., 2022).

Most studies to date have focused on unidirectional waves. However, in the real ocean, waves are directionally spread (i.e., energy travels in multiple directions). Including the directionally spread effect is therefore important. These have been widely studied for flat bathymetries (Lo and Mei, 1987; Gibbs and Taylor, 2005; Barratt et al., 2021). Barratt et al. (2021) simulated wave evolution with steep directionally spread wave groups formed by dispersive focusing and investigated the spectral evolution.

Ducrozet and Gouin (2017) investigated the effect of directionally spread waves propagating over a varying bathymetry and found that the enhancement of extreme wave occurrence is reduced, relative to that found with unidirectional propagation.

The extension of the work on unidirectional waves to directionally spread waves is complex and computationally challenging, and we do not aim to tackle the full problem here. This work is mainly focused on studying the angle of the second-order released wave on the shallower-water side when the directionally spread wave groups propagate over the abrupt depth transition. In previous chapters we have shown that these released second-order waves are an important factor in producing larger waves at depth discontinuities. This angle will be central to any extension of the theoretical

work of Li *et al.* to directional waves and therefore needs to be understood clearly. Additionally, the difference between the propagation angle of the primary wave group and the direction of released second-order free waves also has a potential implication for localised spatial inhomogeneity of random wave fields, leading to deviations from standard prediction models. To study this, we use a fully non-linear potential flow solver to simulate directionally spread wave groups propagating over abrupt depth transitions. In our simulations, the abrupt depth transition is not uniform in y-direction, potentially leading to refraction. Refraction occurs when the direction of the waves is not normal to the depth contours (oblique incidence), and the wave can change direction as it approaches the coast, which is due to depth variation along the wave crest with a corresponding variation in phase speed along the crest. We can clearly observe the refraction of the main wave group in all of our simulation results. However, refraction is well understood, and we are primarily interested in the angle of the released second-order free wave when a wave group passes the abrupt depth transition.

5.2 Numerical methodology

5.2.1 Numerical set up

In this paper, all of the numerical results are obtained using OceanWave3D (OW3D). This code time-marches the classical potential-flow equations, meaning OW3D is a fully nonlinear potential-flow solver (Engsig-Karup et al., 2009). The governing equations and the details of OW3D are briefly introduced in chapter 2. In these chapters, we simulate unidirectional waves propagating over an abrupt depth transition, including the simulations of unidirectional wave groups and unidirectional random waves. However, in this chapter, we simulate directionally spread wave groups propagating over an abrupt depth transition (slope), which is not uniform in the y-direction

leading to an angle with x-direction in the (x, y) plane (top view of the slope).

In the numerical simulation of OW3D, we first define the initial conditions. We define the surface elevation and the velocity potential in the spatial domain. Then we time-march the simulation based on the potential-flow equations. The numerical set up for all of the simulations is the same, the length of the numerical domain in the x-direction, L_x, is 15360 m, with a length of 69 wavelengths for waves on the deeper-water side. The length of the numerical domain in the y-direction, L_y, is 10240 m, with a length of 45 wavelengths. The size of the domain is chosen to ensure the wave group does not interact with the boundary of the domain. The number of nodes on the x-axis, N_x, is 1025 (15 nodes per wavelength) and the number of nodes on the y-axis, N_y, is 513. In addition, there are 9 nodes on the z-axis (vertical). The timestep, Δt, is 0.4 s (30 timesteps per wave period), and the total simulation time is 960 s (2400 timesteps). We followed the grid resolution and time-marching setup from Barratt et al. (2021) to ensure the numerical convergence of our simulations.

Slope angle with the x-direction in the (x, y) plane (α)	$H_{shallow}$	H_{deep}	Gradient of the slope in the x-direction	Gradient of the slope in the y-direction
33°	30 m	150 m	1	1.54
	50 m	150 m	1	1.54
	70 m	150 m	1	1.54
41°	30 m	150 m	1	1.15
	50 m	150 m	1	1.15
	70 m	150 m	1	1.15
53°	30 m	150 m	1	0.75
	50 m	150 m	1	0.75
	70 m	150 m	1	0.75
70°	30 m	150 m	1	0.36
	50 m	150 m	1	0.36
	70 m	150 m	1	0.36

Table 5.1: Details of the different slopes and different bathymetry in the simulations by OW3D

The slopes in the numerical model are detailed in Table 5.1. α is the angle of

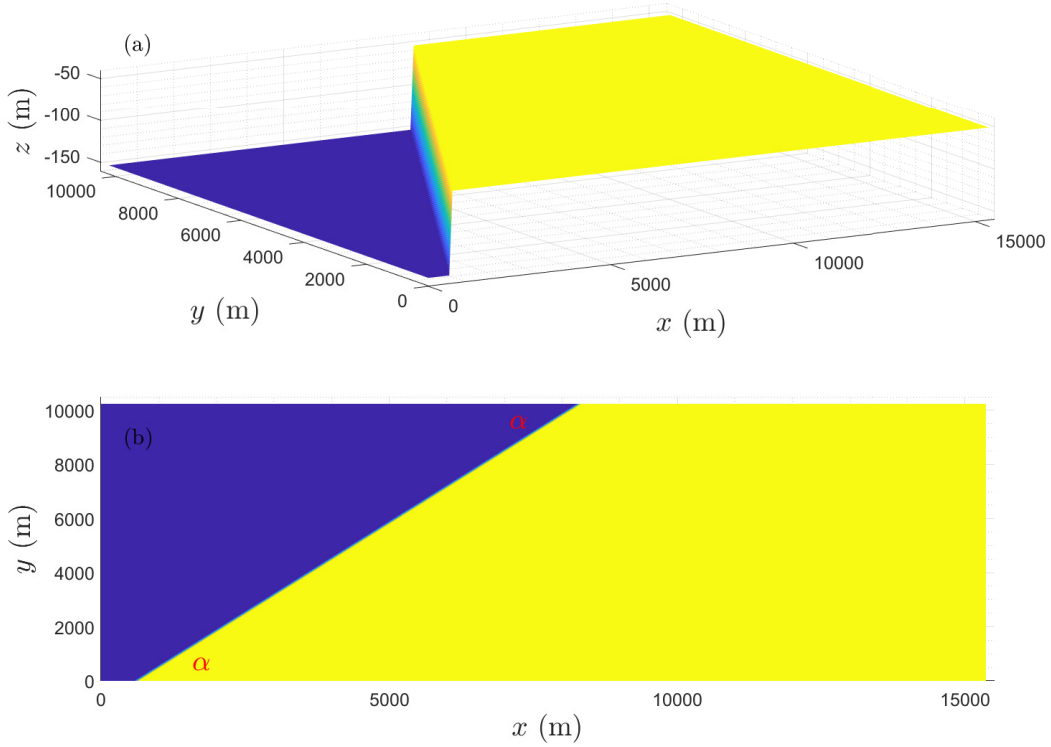


Figure 5.1: Figure of the slope (a) and the top view of the slope (b) for α = 53° slope with $H_{shallow}$ = 50 m case. α indicates the angle of the slope with respect to the x-direction in the (x, y) plane. z indicates the water depth to the mean water level. Yellow region corresponds to the shallower-water side, and blue region is the deeper-water side

the slope with the x-direction in the (x, y) plane (top view of the slope). We use four different slope setups with different angles of α. For each slope, we vary the water depth on the shallower-water side, $H_{shallow}$, from 30 m, 50 m to 70 m, whereas the water depth on the deeper-water side H_{deep} is maintained at 150 m for all of the simulation cases. For all of the cases, the gradient of the slope along the x-direction is fixed to a 1:1 slope (in the (x, z) plane). Our assumption in this chapter, based on the work in the previous chapters, is that the results are not sensitive to the slope gradient and thus we only consider one gradient.

In Figure 5.1, the slope and the bathymetry are shown with α = 53° slope with $H_{shallow}$ = 50 m case. Yellow regions correspond to the shallower-water side and the blue region corresponds to the deeper-water side. For all of the simulations, the shortest distance of deeper-water side along the x-direction in the (x, y) plane is 570 m, and the directionally spread wave is propagating from deeper-water side (blue region) to the shallower-water side (yellow region) (i.e. from left to right).

5.2.2 Input waves

We use directionally spread wave groups for our simulations. These deterministic groups allow us to explore the physics without excessive computational demand and without strong interactions between the waves and the boundary of the domain. In our simulation, we define the initial conditions of the input waves, which include calculations of the surface elevation and the velocity potential at the free surface as done for example in Gibbs and Taylor (2005). The initial conditions are set so that in 15 characteristic wave periods after the start the groups linearly focus if the bathymetry were flat with a depth of 150 m. The initial condition of the surface elevation is shown in Figure 5.2. The peak wavenumber, k_p, is 0.0279 m^{-1}, which corresponds to a characteristic wavelength of 225 m, and the steepness at linear focus with flat bathymetry, Ak_p, is 0.1. Although our results are based on simulations of

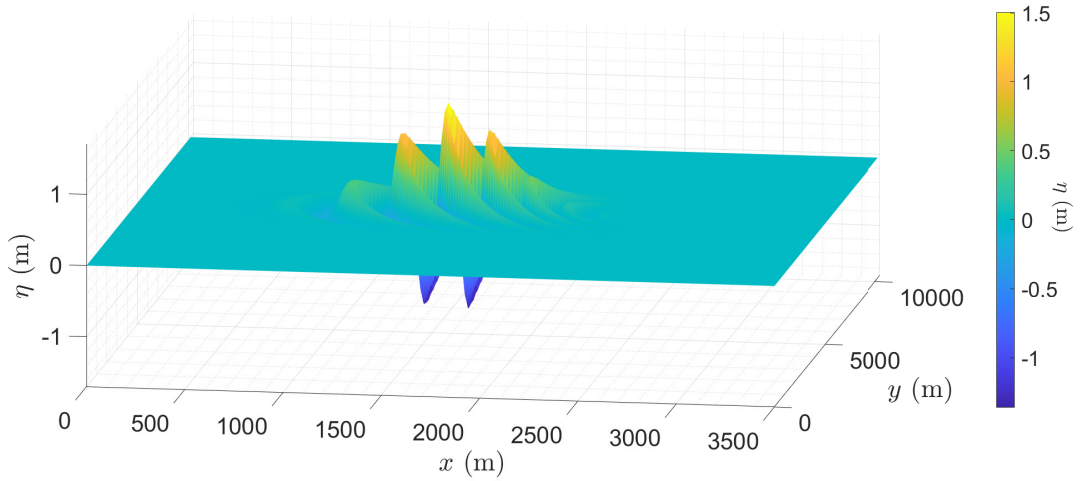


Figure 5.2: Initial condition for the surface elevation for the wave group in OceanWave3D, where η is the surface elevation.

a wave group with Ak_p = 0.1, we also simulate some extra cases for a wave group with Ak_p = 0.3 to examine if steepness impacts our results. The characteristic wave period, T_p, is 12 s. Second-order initial conditions are used based on the simulations of Barratt et al. (2020).

We use 'NewWave' wave groups based on a Gaussian spectrum in wavenumber spectrum. The variance density spectrum $F(k.\theta)$ of the initial conditions can be defined as the product of a wavenumber magnitude spectrum $S(k)$ and a spreading function $D(\theta)$. The Gaussian spectrum, $S(k)$, is given by:

$$S(k) = \exp\left(\frac{-(k-k_p)^2}{2{k_w}^2}\right), \tag{5.1}$$

where k_p is the peak wavenumber, which is 0.0279 m^{-1} in this case. k_w is the spectral width, which is 0.004606 m^{-1}. This follows Gibbs (2004) who fitted this Gaussian spectrum to the peak of a JONSWAP spectrum with peak enhancement of 3.3. The spreading function $D(\theta)$ is given by:

$$D(\theta) = \frac{1}{\sqrt{2\pi}\varsigma}\exp\left(\frac{-\theta^2}{2\varsigma^2}\right), \tag{5.2}$$

with a constant rms spreading parameter (ς) of 15°. The surface elevation of the focused linear event assumes an approximate form expressed in terms of the spatial bandwidths S_x and S_y:

$$\eta(x,y) = Ae^{-\frac{1}{2}S_x^2x^2}e^{-\frac{1}{2}S_y^2y^2}\cos\left(k_px\right), \tag{5.3}$$

where S_x is equivalent to the spectral width of the unidirectional spectrum. S_y is related to the rms spreading angle in radians, σ_{rms}, by $S_y = \sigma_{rms}k_p$. This represents a close approximation to the shape of the linear focused 'NewWave' groups.

5.3 Results

5.3.1 Theories to explain the angle of the second-order released waves

In order to estimate the angle of the released second-order free waves, two theories have been proposed. These are described below.

In the first theory, release-time theory (developed as part of this work), we base the analysis on the difference in space and time between the release of bound waves at different points along the slope. This approach is summarised in Figure 5.3. Suppose we have a wave travelling from left to right which encounters a depth discontinuity which is not at 90 degrees to this wave. Now let us consider two points along this wave in the x-direction. The wave at one of these points will encounter the depth discontinuity first at which point it will release a second-order wave. This second-order wave will travel at the speed defined by the dispersion relationship at given frequency and water depth and is assumed to travel in the same direction as the incident wave. The travel distance of this second-order wave is L_2 in Figure 5.3. The other point on the incident wave will eventually hit the depth discontinuity and release

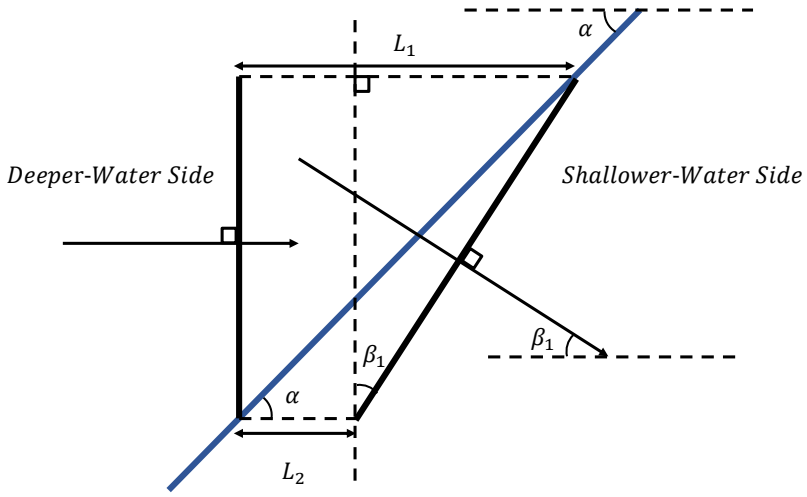


Figure 5.3: Release-time theory to calculate the angle between the released second-order free wave and the x-direction, β_1. α indicates the angle of slope with x-direction in (x, y) plane. L_1 is the propagation distance on the deeper-water side and L_2 is the propagation distance on the shallower-water side.

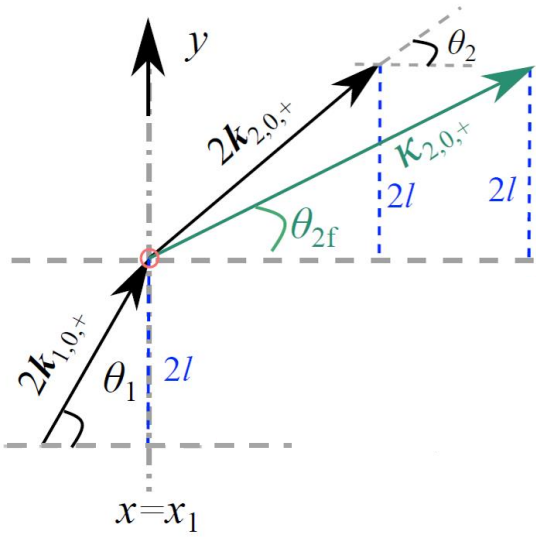


Figure 5.4: Theory of Li *et al.*, the angle relation in terms of the angle of second-order bound waves before and after the slope and the angle of second-order released waves. $2k_{1,0,}+$ and θ_1 is the wavenumber and the angle of the second-order bound wave before the slope, respectively. $2k_{2,0,}+$ and θ_2 is the wavenumber and the angle of the second-order bound wave after the slope, respectively. $\kappa_{2,0,}+$ is the wavenumber of the second-order released free wave and θ_{2f} is the angle between the second-order released wave and the directional normal to the slope in the (x, y) plane.

a second-order wave, corresponding to travel distance L_1 in Figure 5.3. However, this second-order wave will not be aligned with the one released by the first wave. Hence an angle can be calculated at which these will propagate. Geometry then allows the following formula to be derived for the angle β_1 shown in Figure 5.3:

$$\beta_1 = \tan^{-1}\left(\frac{1}{\tan\alpha}\cdot\left(1-\frac{c_2}{c_1}\right)\right), \tag{5.4}$$

where α is the angle between the slope and the x-direction in the (x, y) plane and in our case, α is 33°, 41°, 53° or 70°. c_1 is the phase speed of the first-order wave on deeper-water side and c_2 is the phase speed of released second-order wave on shallower-water side.

This theory has some analogues to Snell's law which is widely used for predictions of refraction in media with different velocities. However, here we are comparing the speed on the linear components and the speed of the released second-order sum components rather than just the speed of the fundamental wave as would classically be done in applying Snell's law.

The second approach is described in a poster by Li et al. (2022a) and shown in Figure 5.4 from which the angle of released second-order waves can be calculated. In the theory of Li *et al.*, waves are traveling from left to right of the figure at an angle to depth discontinuity, which is indicated by the vertical line. In Figure 5.4, $2k_{1,0,}+$ is the wavenumber of the second-order bound wave before the slope and the angle, θ_1, is consistent with the main wave group. $2k_{2,0,}+$ is the wavenumber of the second-order bound wave after the slope and the angle, θ_2, is also consistent with the main wave group after the slope. $\kappa_{2,0,}+$ is the wavenumber of the released second-order free wave, and θ_{2f} is the angle between the second-order released wave and the direction normal to the slope in the (x, y) plane. Based on the angle relation, the angle between the second-order released wave and the x-direction (β_2) can be calculated.

In Figure 5.5, the theoretical angle of the released second-order free wave with the

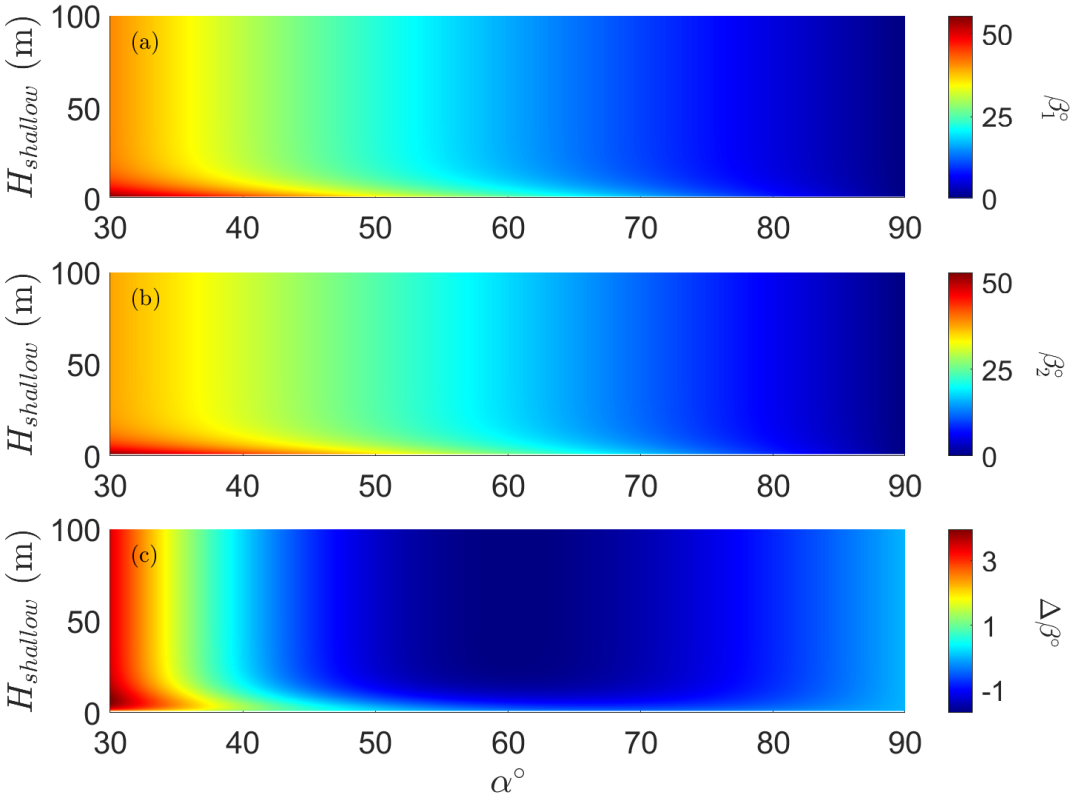


Figure 5.5: The comparison of the theoretical angle of the released second-order free wave calculated by release-time theory (a) and Li *et al.* (b). $H_{shallow}$ is the water depth on the shallower-water side. α is the angle of the slope with the x-direction in the (x, y) plane. β_1 and β_2 are the angle of the released second-order free wave with the x-direction in the (x, y) plane, calculated by release-time theory and Li *et al.*, respectively. $\Delta\beta$ in (c) is the difference of the angle of the released second-order free wave calculated by these two theories ($\Delta\beta = \beta_1 - \beta_2$).

x-direction in the (x, y) plane is calculated by release-time theory (β_1) and Li *et al.* (β_2), shown in Figure 5.5 (a) and 5.5 (b), respectively. In Figure 5.5, the angle of the released second-order free wave is determined by water depth on the shallower-water side ($H_{shallow}$) and the angle of the slope (α), and the relationship is presented. The angle predicted by both theories is very similar. The angle of the released second-order free wave is mainly determined by the angle of the slope with the x-direction and the water depth on the shallower-water side has a significant influence only for very shallow water depth. In Figure 5.5 (c), the difference of the angles of the released second-order free wave ($\Delta\beta = \beta_1 - \beta_2$) is shown, which is calculated by the difference of these two theories.

It is remarkable that by making different assumptions extremely similar, although not identical, results are predicted.

5.3.2 Numerical results of directionally spread waves

We consider 12 cases with different slopes and different water depth on the shallower-water side, which are shown in Table 5.1. We focus on the angle of the released second-order free waves. In Figure 5.6, the initial condition is shown. In Figure 5.7, the numerical result of 640 s for the 53° slope with $H_{shallow} = 50$ m case is presented (top view). The released second-order free wave is approximately located at $x = 6000$ m. The angle (β) between the released second-order free wave and the x-direction in the (x, y) plane is calculated for all of the simulation cases. To calculate the angle, β, we first find the tangent line of the wave front for the second-order released wave group. Then, β is the angle between line normal to the tangent line and the x-direction, shown in Figure 5.7. Based on this approach, the angles of the released second-order free wave for all of the simulations are calculated and shown in Figure 5.8. In Figure 5.8, the numerical results of the angles are compared with two theories previously introduced in Section 5.3.1.

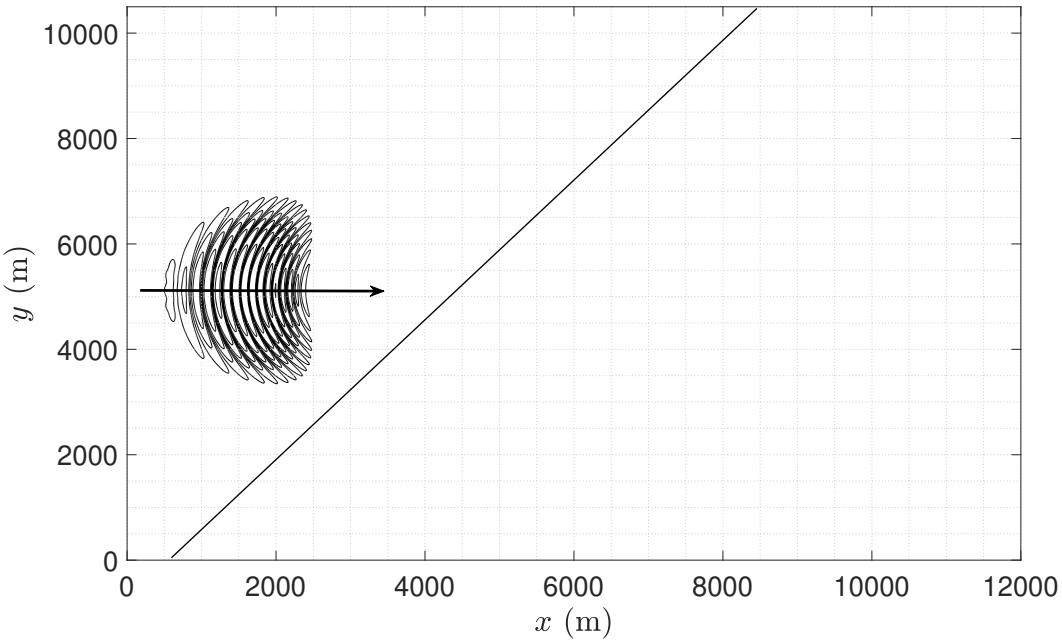


Figure 5.6: Contour plot of the initial condition. Slope is indicated by the black line. The contour plot is in an interval of surface elevation η between -0.5 m to 0.5 m. Arrow indicates the moving direction.

We find the angle of the released second-order free wave (β) is mainly determined by the angle of the slope with respect to the x-direction (α). When the angle between the slope and the x-direction in the (x, y) plane increases, the angle between the second-order released wave and the x-direction decreases. In addition, we find the water depth on shallower-water side, $H_{shallow}$, has small influence on the angle of the second-order released waves for the range considered. Compared with the two theories in Section 5.3.1, we find the agreement between the numerical results of angles and the theoretical angles is excellent. Given the difference between the theoretical results is small it is impossible to say which is a better fit to the numerical results.

We present the results in terms of Ak_p = 0.1 cases as it minimises the non-linear physics but is sufficiently non-linear to see the released wave at the step. We also investigate the influence of the wave steepness on the angle of the released second-order free waves, we simulate two extra cases by using a wave group with steepness

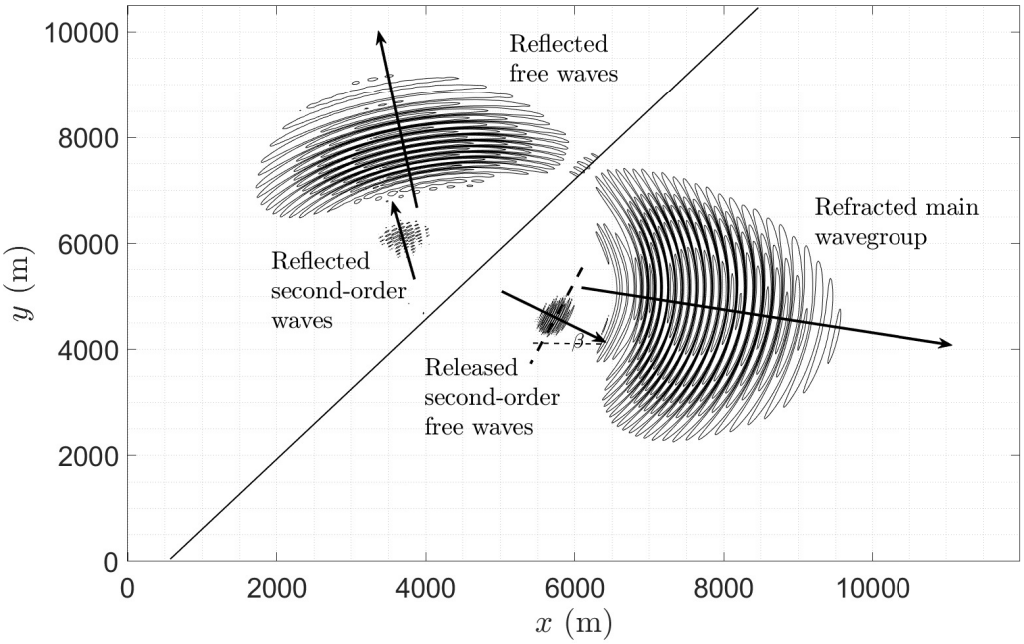


Figure 5.7: Contour plot of the numerical result of 1600_{th} timestep for 53° angle slope with 50 m $H_{shallow}$ case. β indicates the angle between the released second-order free wave and the x-direction in the (x, y) plane (top view of the waves). Slope is indicated by the black line. The contour plot is in an interval of surface elevation η between -0.5 m to 0.5 m. Arrow indicates the moving direction.

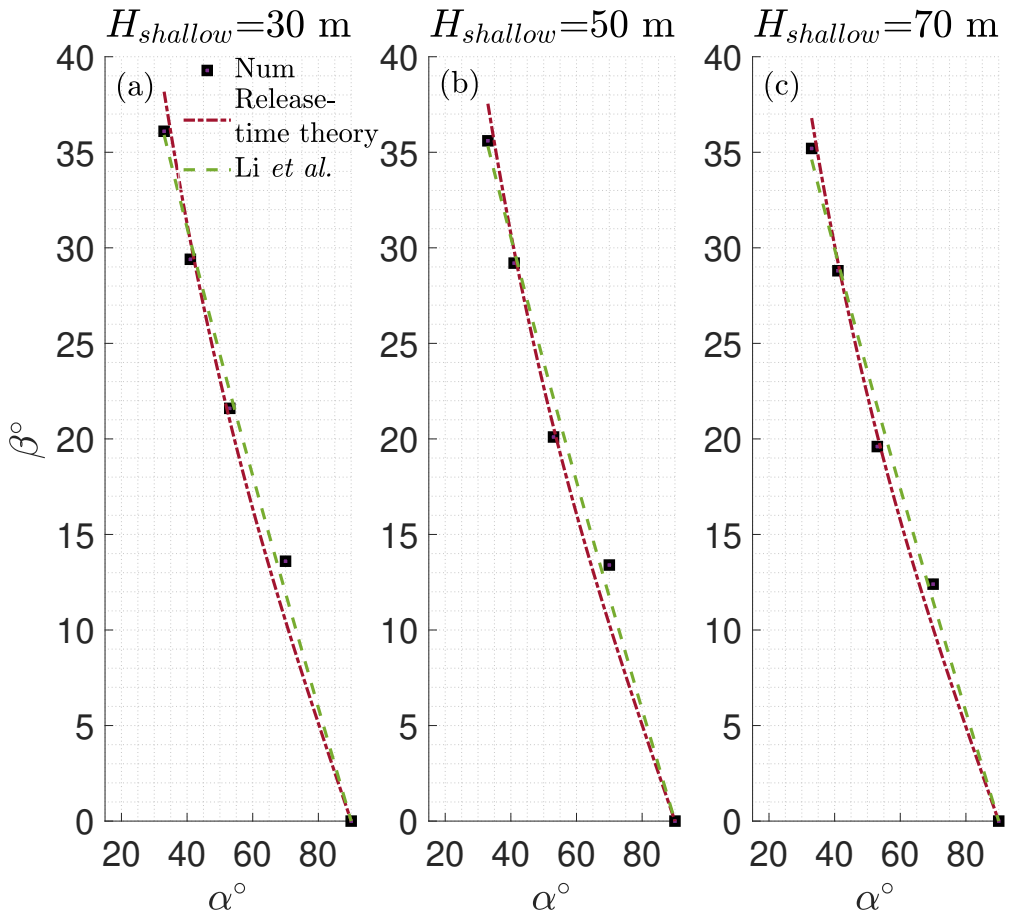


Figure 5.8: The comparison of the angle of the released second-order free waves calculated by numerical simulation, release-time theory or Li *et al.* α is the angle of the slope with the x-direction in the (x, y) plane and β is the angle of the released second-order free wave in the (x, y) plane. $H_{shallow}$ is the water depth on the shallower-water side.

Ak_p = 0.3 for verification and we find there is little influence on the angle of the released second-order free waves (around 1% difference).

5.4 Conclusions

This paper primarily focuses on the problem of directionally spread waves propagating over abrupt depth transitions. We investigate the angle of the released second-order free waves when the main wave group propagates over the slope. The existence of the second-order released wave is consistent with the theory by Li et al. (2021b), which can lead to the formation of the rogue waves.

We have run 12 cases with different slopes and water depths on the shallower-water side using a fully non-linear potential-flow solver, OceanWave3D. We find the angle between the released second-order free wave and the x-direction decreases when the angle of the slope with the x-direction increases. In addition, we find the angle of the second-order released wave is much less influenced by the water depth on the shallower-water side, at least for the range of water depth considered herein. We compare our results with two theoretical models and we find the agreement with theory is good. This study investigates the angle of the released second-order free wave when directionally spread wave group pass an abrupt depth transition and the results are helpful to many extension works related to directionally spread sea-states. Either theoretical model may be used to develop a theory further.

Chapter 6

Conclusions and Recommendations

Investigating the statistics and kinematics of rogue waves is extremely important as it ultimately determines the wave loading and safety of the offshore infrastructures. Wave propagation over an abrupt depth transition is known as one of the possible mechanisms that can provoke rogue waves. Many offshore structures, such as offshore wind turbines, are located at the top of the slope. Thus, studying how the abrupt depth transition provoke the rogue waves and the waves kinematics under the free surface after the slope is essential. In this study, we conduct three different types of simulations with different initial conditions of waves, including unidirectional wavegroups, unidirectional random waves and directionally spread wavegroups, which is shown in Table 1.1. Our main findings and the conclusions are explained as follows:

1. The convergence test and validation of OceanWave3D.
2. The analysis of wave kinematics and wave loading on the structures.
3. The analysis of the angle of the release second-order free waves.

6.1 The convergence test and validation of OceanWave3D

In chapter 3, we conduct a thorough convergence test to evaluate the numerical accuracy of OceanWave3D. Firstly, we simulate the wavegroups propagation on a flat bathymetry by Oceanwave3D and analyze the influence of different values of parameters in OceanWave3D on the numerical results, including spatial and temporal discretisation. We evaluate the numerical accuracy by comparing with the base case, which has the finest resolution. We find the accuracy of OceanWave3D is primarily dominated by the timestep.

In chapter 3, we simulate wavegroups propagating over varying bathymetries. To test the numerical accuracy, we utilise the reversibility properties of the governing equations. We run the simulations forward in time up to the slope, before reversing the sign of time step to run the simulations back to initial conditions. The numerical accuracy can be obtained by comparing the difference between the initial conditions and the result at the end of the backward simulation. Based on the difference between these two wavegroups, we find the numerical error is small and the agreement between these two wavegroups is satisfactory. Thus, we have confidence that OceanWave3D can solve the governing equations accurately for waves propagation over a slope.

Apart from the convergence test, in chapter 3, we conduct the validation of OceanWave3D by comparing with the experimental results, in terms of the unidirectional wavegroups propagation over a slope. We find the agreement between numerical wavegroups and experimental wavegroups is satisfactory, although some mismatches are found on the third-order harmonic waves. The cause of this discrepancy is still unclear. In chapter 4, we conduct the validation tests for random waves propagation over a slope. The agreement between numerical and experimental results is also satisfactory.

Apart from deterministic waves, in chapter 4, we also compare the exceedance probability of wave height and the average shape of extreme events between the numerics and experimental results. We find the agreement is satisfactory in both exceedance probability and the average shape of extreme events.

Based on our convergence test and the validation, we have confidence that OceanWave3D is numerically accurate for both wavegroup simulations and random wave simulations. In addition, OceanWave3D can reproduce experimental results accurately and therefore can capture the important real-world physics.

6.2 The analysis of wave kinematics and wave loading on the structures

In chapter 3, we analyze how the kinematics of the wavegroups change after the top of the slope. We find the total velocity has a very local increase at the top of the slope and the maximum velocity occurs some wavelengths after the top of the slope. Moreover, we also consider the wave loading and overturning moment based on the wave kinematics obtained previously. We use the Morison's equation to estimate the wave loading and we compare the wave loading calculated by non-linear simulation results and linear simulation results. We find that loads on the offshore structures are significantly enhanced in the non-linear simulation, which means the enhancement is the result of non-linear physics as waves pass over a slope.

In chapter 4, we simulate the propagation of random waves pass over a slope and analyze the wave kinematics. Non-linear simulations and linear simulations for random waves are also studied here. In addition, two different types of slope, 1:1 slope and 1:3 slope are investigated. In the non-linear simulations, we find the overall trend of wave loads is similar for both 1:1 slope case and 1:3 slope case. The enhanced loads for these two cases last for several wavelengths after the top of the slope. Afterwards,

this enhancement becomes weaker and the loads reduce to a steady state. In the steady state region, the results of non-linear simulations become consistent with the results of linear simulations. In addition, we find the enhanced overturning moments has an increase of approximately 20 % after the top of the slope for non-linear simulations whereas this increase does not occur in linear simulations. These results suggest that extra care is needed when designing ocean infrastructures at the top of the slopes.

6.3 The analysis of the angle of the release second-order free waves.

In chapter 5, we simulate the directionally spread wavegroups propagating over abrupt depth transitions. We have 12 simulations with different slopes and different water depth on the shallower-water region. The slope is positioned at an angle with the x-direction. These slopes have four different angles with the x-direction in the (x, y) plane, which are 33°, 41°, 53° and 70°. For each angle, the water depth on the shallower-water region also varies from 30 m, 50 m to 70 m. Based on our simulation results, we can observe the released second-order free waves when directionally spread wavegroups pass over the slopes, which is consistent with the theory proposed by Li et al. (2021a). Moreover, we find the angle of the released second-order free waves is primarily depends on the angle of the slope with respect to the x-direction in the (x, y) plane and are less sensitive to the water depth on the shallower-water region, at least for the range of water depth considered herein. We find if the angle between the x-direction and the slope increases, the propagation angle of the released second-order free wave with the x-direction decreases. We compare our numerical results with two theoretical models. We find the agreement between the released second-order free wave and both of the theories are satisfactory for angles and water depths tested

herein.

6.4 Recommendations for the future work

6.4.1 Analysis of directionally spread random waves

Our directionally spread results are only for wavegroups. However, analysis of random waves is also important as lots of wave statistics is based on the random waves results. For example, average shape of extreme events can be analysed, which has a significant impact on extreme force estimations and it is important when calculating the response of the ship and wave slamming effects for extreme events. In addition, the exceedance probability of wave height can be studied, as the slope can significantly increase the probability of extreme waves at the top of the slope.

6.4.2 Analysis of wave kinematics for directionally spread random waves

In the past work, many studies is focused on the investigation of the free surface wave statistics whereas much less work is related to the wave kinematics. However, the wave kinematics is important as it is closely related to the wave loading on offshore structures such as offshore wind turbine. Lawrence et al. (2021a) have investigated the wave kinematics, developing a new method for the calculation of water-particle kinematics based on the fully nonlinear Variational Boussinesq, which has been applied to waves propagation over slope. The statistics of wave kinematics in long-crested irregular waves propagating over a shoal is studied by Lawrence et al. (2021b) and the influence of different slope areas is discussed. In the future work, the analysis of wave kinematics for directionally spread random waves can be the next step. The velocity of water particle can be studied for cases with different mean wave

propagation direction and at various water depths. Based on the horizontal velocity, the wave loading on a structure can be calculated by Morison's equation. In addition, except the analysis of the cylinder, different shape of the structure can be investigated at the top of the slope and different slopes can also be studied.

The process of wave propagating over an abrupt depth transition is extensively studied numerically and experimentally. In the numerics and experiments, the influence of the abrupt depth transition on the rogue waves is verified and well understood. However, there is not enough field data which describes this process. Whether the same results can be obtained in field data is unclear. It is also unclear that what is the statistics based on the field data. Therefore, investigating the field data is essential to understand wave propagating over an abrupt depth transition, which can be the future work.

References

Adcock TAA, Taylor PH (2009) Focusing of unidirectional wave groups on deep water: an approximate nonlinear Schrödinger equation-based model. Proceedings of the Royal Society A: Mathematical, Physical and Engineering Sciences 465(2110):3083–3102

Adcock TAA, Taylor PH (2014) The physics of anomalous ('rogue') ocean waves. Reports Prog Phys 77(10):105901

Airy GB (1845) Tides and waves. B. Fellowes

Al-Humoud J, Tayfun M, Askar H (2002) Distribution of nonlinear wave crests. Ocean engineering 29(15):1929–1943

Arany L, Bhattacharya S, Macdonald JHG, Hogan SJ (2016) Closed form solution of Eigen frequency of monopile supported offshore wind turbines in deeper waters incorporating stiffness of substructure and SSI. Soil Dynamics and Earthquake Engineering 83:18–32

Baldock TE, Swan C, Taylor PH (1996) A laboratory study of nonlinear surface waves on water. Philos Trans Royal Soc A Math Phys Eng Sci 354(1707):649–676

Barber NF, Ursell F (1948) The generation and propagation of ocean waves and swell. i. wave periods and velocities. Philosophical Transactions of the Royal Society of London Series A, Mathematical and Physical Sciences 240(824):527–560

Barratt D, Bingham HB, Adcock TAA (2020) Nonlinear evolution of a steep, focusing wave group in deep water simulated with OceanWave3D. Journal of Offshore Mechanics and Arctic Engineering 142(2):021201

Barratt D, Bingham HB, Taylor PH, Van Den Bremer TS, Adcock TAA (2021) Rapid spectral evolution of steep surface wave groups with directional spreading. J Fluid Mech 907

Barratt D, van den Bremer TS, Adcock TAA (2022) The impact of the spectral tail on the evolution of the kurtosis of random seas. Journal of Offshore Mechanics and Arctic Engineering 144(6):061703

Bateman WJ, Swan C, Taylor PH (2003) On the calculation of the water particle kinematics arising in a directionally spread wavefield. Journal of Computational Physics 186(1):70–92

Beji S, Battjes J (1993) Experimental investigation of wave propagation over a bar. Coastal Engineering 19(1-2):151–162

Bingham HB, Zhang H (2007) On the accuracy of finite-difference solutions for nonlinear water waves. J Eng Math 58(1):211–228

Bitner EM (1980) Non-linear effects of the statistical model of shallow-water wind waves. Applied Ocean Research 2(2):63–73

Boccotti P (1983) Some new results on statistical properties of wind waves. Applied Ocean Research 5(3):134–140

Bolles CT, Speer K, Moore MNJ (2019) Anomalous wave statistics induced by abrupt depth change. Physical review fluids 4(1):011801

Cartwright DE, Longuet-Higgins MS (1956) The statistical distribution of the maxima of a random function. Proc R Soc A Math Phys Eng Sci 237(1209):212–232

Cavanie A, Arhan X, Ezraty X (1976) A statistical relationship between individual heights and periods of storm waves

Chau FP, Eatock Taylor R (1992) Second-order wave diffraction by a vertical cylinder. Journal of Fluid Mechanics 240:571–599

Cherneva Z, Petrova P, Andreeva N, Soares CG (2005) Probability distributions of peaks, troughs and heights of wind waves measured in the black sea coastal zone. Coastal Engineering 52(7):599–615

Clamond D, Fructus D, Grue J, Kristiansen Ø (2005) An efficient model for three-dimensional surface wave simulations. part ii: Generation and absorption. Journal of computational physics 205(2):686–705

Dean RG, Dalrymple RA (1991) Water wave mechanics for engineers and scientists, vol 2. World Scientific Publishing Company

Didenkulova I (2011) Shapes of freak waves in the coastal zone of the Baltic Sea (Tallinn Bay)

Didenkulova I, Anderson C (2010) Freak waves of different types in the coastal zone of the baltic sea. Natural Hazards and Earth System Sciences 10(9):2021–2029

Draper L (1971) Severe wave conditions at sea. J Inst Navig 24(3):273–277

Draycott S, Li Y, Stansby PK, Adcock TAA, van den Bremer TS (2022) Harmonic-induced wave breaking due to abrupt depth transitions: An experimental and numerical study. Coastal Engineering 171:104041

Ducrozet G, Gouin M (2017) Influence of varying bathymetry in rogue wave occurrence within unidirectional and directional sea-states. J Ocean Eng Sci 3(4):309–324

Dysthe KB, Krogstad HE, Müller P (2008) Oceanic rogue waves. Annu Rev Fluid Mech 40(1):287–310

Eeltink D, Branger H, Luneau C, He Y, Chabchoub A, Kasparian J, van den Bremer T, Sapsis T (2022) Nonlinear wave evolution with data-driven breaking. Nature communications 13(1):2343

Engsig-Karup AP, Bingham HB, Lindberg O (2009) An efficient flexible-order model for 3D nonlinear water waves. J Comput Phys 228(6):2100–2118

Feng X, Taylor PH, Dai S, Day A, Willden RHJ, Adcock TAA (2020) Experimental investigation of higher harmonic wave loads and moments on a vertical cylinder by a phase-manipulation method. Coastal Engineering 160:103747

Flanagan JD, Dias F, Terray E, Strong B, Dudley J, et al. (2016) Extreme water waves off the west coast of ireland: analysis of adcp measurements. In: The 26th International Ocean and Polar Engineering Conference, International Society of Offshore and Polar Engineers

Gibbs RH (2004) Walls of water on the open ocean. PhD thesis, University of Oxford

Gibbs RH, Taylor PH (2005) Formation of walls of water in 'fully'nonlinear simulations. Applied Ocean Research 27(3):142–157

Gramstad O, Zeng H, Trulsen K, Pedersen GK (2013) Freak waves in weakly nonlinear unidirectional wave trains over a sloping bottom in shallow water. Physics of Fluids 25(12):122103

Grue J (1992) Nonlinear water waves at a submerged obstacle or bottom topography. Journal of Fluid Mechanics 244:455–476

Grue J (2011) Two phenomena: Honji instability, and ringing of offshore structures. Theor App Mech Lett 1(6):062001

Hasselmann K, Barnett TP, Bouws E, Carlson H, Cartwright DE, Enke K, Ewing J, Gienapp A, Hasselmann D, Kruseman P, et al. (1973) Measurements of wind-

wave growth and swell decay during the joint north sea wave project (jonswap). Ergaenzungsheft zur Deutschen Hydrographischen Zeitschrift, Reihe A

Haver S (2001) Evidences of the existence of freak waves. In: Rogue waves, Ifremer Brest, pp 129–140

Haver S (2004) A possible freak wave event measured at the draupner jacket january 1 1995. In: Rogue waves, vol 2004, pp 1–8

Holthuijsen LH (2010) Waves in oceanic and coastal waters. Cambridge university press

Huseby M, Grue J (2000) An experimental investigation of higher-harmonic wave forces on a vertical cylinder. Journal of fluid Mechanics 414:75–103

Jensen TG (1998) Open boundary conditions in stratified ocean models. Journal of Marine Systems 16(3-4):297–322

Kallehave D, Byrne BW, LeBlanc Thilsted C, Mikkelsen KK (2015) Optimization of monopiles for offshore wind turbines. Philosophical Transactions of the Royal Society A: Mathematical, Physical and Engineering Sciences 373(2035):20140100

Karin Magnusson A, Donelan MA (2013) The andrea wave characteristics of a measured north sea rogue wave. Journal of Offshore Mechanics and Arctic Engineering 135(3)

Kashima H, Hirayama K, Mori N (2014) Estimation of freak wave occurrence from deep to shallow water regions. Coastal Engineering Proceedings 1(34):36

Kharif C, Pelinovsky E (2003) Physical mechanisms of the rogue wave phenomenon. Eur J Mech 22(6):603–634

Klahn M, Madsen PA, Fuhrman DR (2021) On the statistical properties of inertia and drag forces in nonlinear multi-directional irregular water waves. Journal of Fluid Mechanics 916

Lawrence C, Gramstad O, Trulsen K (2021a) Variational boussinesq model for kinematics calculation of surface gravity waves over bathymetry. Wave Motion 100:102665

Lawrence C, Trulsen K, Gramstad O (2021b) Statistical properties of wave kinematics in long-crested irregular waves propagating over non-uniform bathymetry. Physics of Fluids 33(4):046601

Li Y, Draycott S, Adcock TAA, van den Bremer TS (2021a) Surface wavepackets subject to an abrupt depth change. Part 2. Experimental analysis. Journal of Fluid Mechanics 915

Li Y, Draycott S, Zheng Y, Lin Z, Adcock TAA, Van Den Bremer TS (2021b) Why rogue waves occur atop abrupt depth transitions. Journal of Fluid Mechanics 919

Li Y, Zheng Y, Lin Z, Adcock TAA, van den Bremer TS (2021c) Surface wavepackets subject to an abrupt depth change. Part 1. Second-order theory. Journal of Fluid Mechanics 915

Li Y, Liang H, Draycott S (2022a) Weakly nonlinear surface gravity waves atop a submerged bar and trench: the wave dynamics and kinematics

Li Z, Tang T, Draycott S, Li Y, van den Bremer T, Adcock T (2022b) On rogue waves generated by abrupt depth transitions. In: International Conference on Offshore Mechanics and Arctic Engineering, American Society of Mechanical Engineers, vol 85901, p V05BT06A063

Li Z, Tang T, Li Y, Draycott S, van den Bremer TS, Adcock TA (2022c) Wave loads on ocean infrastructure increase as a result of waves passing over abrupt depth transitions. Journal of Ocean Engineering and Marine Energy pp 1–9

Lindgren G, et al. (1970) Some properties of a normal process near a local maximum. Annals of Mathematical Statistics 41(6):1870–1883

Liu PC (2007) A chronology of freauqe wave encounters. Geofizika 24(1):57–70

Lo E, Mei CC (1985) A numerical study of water-wave modulation based on a higher-order nonlinear Schrödinger equation. Journal of Fluid Mechanics 150:395–416

Lo EY, Mei CC (1987) Slow evolution of nonlinear deep water waves in two horizontal directions: A numerical study. Wave motion 9(3):245–259

Longuet-Higgins MS (1952) On the statistical distribution of the height of sea waves. J Mar Res 11:245–266

Massel SR (1983) Harmonic generation by waves propagating over a submerged step. Coastal Engineering 7(4):357–380

Mendes S, Scotti A, Brunetti M, Kasparian J (2022) Non-homogeneous analysis of rogue wave probability evolution over a shoal. Journal of Fluid Mechanics 939

Monsalve E, Maurel A, Pagneux V, Petitjeans P (2022) Nonlinear waves passing over rectangular obstacles: Multimodal method and experimental validation. Fluids 7(5):145

Monsalve Gutiérrez E (2017) Experimental study of water waves: nonlinear effects and absorption. PhD thesis, Université Pierre & Marie Curie-Paris 6

Mori N, Yasuda T (2002) A weakly non-gaussian model of wave height distribution for random wave train. Ocean Engineering 29(10):1219–1231

Morison JR, , Johnson JW, Schaaf SA (1950) The force exerted by surface waves on piles. Journal of Petroleum Technology 2(05):149–154

Müller P, Garrett C, Osborne A (2005) Rogue waves. Oceanography 18(3):66

Ochi MK, Wang WC (1985) Non-gaussian characteristics of coastal waves. In: Coastal Engineering 1984, pp 516–531

Onorato M, Residori S, Bortolozzo U, Montina A, Arecchi FT (2013) Rogue waves and their generating mechanisms in different physical contexts. Physics Reports 528(2):47–89

Rainey RCT (1989) A new equation for calculating wave loads on offshore structures. Journal of Fluid Mechanics 204:295–324

Rice SO (1944) Mathematical analysis of random noise. The Bell System Technical Journal 23(3):282–332

Roorda EP (2019) The wreck of the uss memphis in the dominican republic. In: Oxford Research Encyclopedia of Latin American History

Sergeeva A, Pelinovsky E, Talipova T (2011) Nonlinear random wave field in shallow water: variable Korteweg-de Vries framework. Natural Hazards and Earth System Sciences 11(2):323–330

Slocum J (1917) Sailing alone around the world. Century Company

Tang T, Adcock TAA (2021) The influence of finite depth on the evolution of extreme wave statistics in numerical wave tanks. Coastal Engineering 166:103870

Tang T, Xu W, Barratt D, Bingham HB, Li Y, Taylor PH, Van Den Bremer TS, Adcock TAA (2021) Spatial evolution of the kurtosis of steep unidirectional random waves. Journal of Fluid Mechanics 908

Tromans PS, Anaturk AR, Hagemeijer P, et al. (1991) A new model for the kinematics of large ocean waves-application as a design wave. In: The first international offshore and polar engineering conference, International Society of Offshore and Polar Engineers

Trulsen K, Zeng H, Gramstad O (2012) Laboratory evidence of freak waves provoked by non-uniform bathymetry. Physics of Fluids 24(9):097101

Trulsen K, Raustøl A, Jorde S, Rye LB (2020) Extreme wave statistics of long-crested irregular waves over a shoal. Journal of Fluid Mechanics 882

Viotti C, Dias F (2014) Extreme waves induced by strong depth transitions: Fully nonlinear results. Physics of Fluids 26(5):051705

Whalin RW (1971) The limit of applicability of linear wave refraction theory in a convergence zone. Waterways Experiment Station

Xie C, Choi Y, Rongère F, Clément AH, Delhommeau G, Babarit A (2018) Comparison of existing methods for the calculation of the infinite water depth free-surface Green function for the wave–structure interaction problem. Applied Ocean Research 81:150–163

Zakharov VE (1968) Stability of periodic waves of finite amplitude on the surface of a deep fluid. Journal of Applied Mechanics and Technical Physics 9(2):190–194

Zang J, Taylor PH, Morgan G, Stringer R, Orszaghova J, Grice J, Tello M (2010) Steep wave and breaking wave impact on offshore wind turbine foundations–ringing re-visited. 25th Int Workshop Water Waves Floating Bodies, Harbin, China pp 9–12

Zeng H, Trulsen K (2012) Evolution of skewness and kurtosis of weakly nonlinear unidirectional waves over a sloping bottom. Natural Hazards and Earth System Sciences 12(3):631–638

Zhang J, Benoit M, Kimmoun O, Chabchoub A, Hsu HC (2019) Statistics of extreme waves in coastal waters: large scale experiments and advanced numerical simulations. Fluids 4(2):99

Zheng YK, Lin ZL, Li Y, Adcock TAA, Li Y, van den Bremer TS (2020) Fully nonlinear simulations of extreme waves provoked by strong depth transitions: the effect of slope. Phys Rev Fluids 5(064804)

Appendix A

Governing equations for OW3D

OceanWave3D solves the potential-flow equations. The fluid velocity (u,v,w) can be calculated by the gradient of a scalar velocity potential $\phi(x, y, z, t)$

$$(u, v, w) = (\nabla\phi, \partial_z\phi), \tag{A.1}$$

In which $\nabla = (\partial_x, \partial_y)$ is the horizontal gradient operator. Based on the equations established by Zakharov (1968), the kinematic and dynamic free surface boundary conditions (given in equations (A.2) and (A.3)) can be expressed by using the chain rule on the nonlinear version of Bernoulli equation and nonlinear kinematic boundary condition.

$$\partial_t\eta = -\nabla\eta\cdot\nabla\widetilde{\phi} + \widetilde{w}(1 + \nabla\eta\cdot\nabla\eta), \tag{A.2}$$

$$\partial_t\widetilde{\phi} = -g\eta - \frac{1}{2}(\nabla\widetilde{\phi}\cdot\nabla\widetilde{\phi} - \widetilde{w}^2(1 + \nabla\eta\cdot\nabla\eta)), \tag{A.3}$$

In which $\widetilde{\phi} = \phi(x, y, \eta, t)$ is the velocity potential at the free surface ($z = \eta$), and $\widetilde{w} = \partial_z\phi|_{z=\eta}$ is the vertical velocity at the free surface. In order to obtain the exact value of the vertical velocity in a specific time, the Laplace equation in the fluid

volume is required to be solved, together with the kinematic and dynamic boundary conditions.